



Cite this: *Phys. Chem. Chem. Phys.*,
2025, 27, 9429

Exploring the influence of M-anion modifications on the physical properties of lead-free novel halide inorganic compounds Ba_3MCl_3 ($\text{M} = \text{N}, \text{P}, \text{As}, \text{Sb}$)

Md. Al Ijajul Islam,^a Md. Ferdous Rahman,^{id} *^a Tanvir Al Galib,^a
Mustafa K. A. Mohammed,^{id} *^b Sagar Bhattarai^{id} ^{ce} and Ahmad Irfan^d

This study investigates the effects of M-anion modifications on lead-free halide inorganic compounds, specifically Ba_3MCl_3 ($\text{M} = \text{N}, \text{P}, \text{As}, \text{Sb}$), using DFT and SCAPS-1D software. It focuses on analyzing their optical, electronic, and structural properties. The lattice parameters for Ba_3MCl_3 were found to be $a = 6.14, 6.44, 6.51, \text{ and } 6.69 \text{ \AA}$, respectively, which is consistent with previous research. Initially, GGA with the PBE functional theory was used. The materials displayed semiconductor characteristics, with direct band gaps of 0.551 eV for Ba_3NCl_3 , 0.927 eV for Ba_3PCl_3 , 0.980 eV for Ba_3AsCl_3 , and 0.996 eV for Ba_3SbCl_3 . Optical characteristics such as absorption, loss function, dielectric function, electrical conductivity, reflectance, and refractive index were also examined. Additionally, the SCAPS-1D software was exploited to thoroughly estimate the efficiency of absorber-based PV cell structures Ba_3NCl_3 , Ba_3PCl_3 , Ba_3AsCl_3 , and Ba_3SbCl_3 with a CdS ETL layer at varying thicknesses, defect densities, and doping levels. QE and $J-V$ characteristics were assessed, with maximum PCEs of 23.06%, 19.93%, 17.12%, and 15.71% for Ba_3NCl_3 , Ba_3PCl_3 , Ba_3AsCl_3 , and Ba_3SbCl_3 , respectively. These computational findings offer valuable insights for developing efficient, lead-free, durable, and cost-effective solar cells based on Ba_3MCl_3 compounds.

Received 21st December 2024,
Accepted 7th April 2025

DOI: 10.1039/d4cp04812a

rsc.li/pccp

1. Introduction

As the global population grows and industrialization progresses, the demand for energy continues to rise. To meet this demand sustainably, renewable energy sources are essential. The urgent issue revolves around the increasing need for advanced photovoltaic cells, optoelectronics, and electronic gadgets, especially as population growth intensifies energy shortages.^{1–4} Organic–inorganic hybrid PSCs have made considerable development in the construction of devices and control elements because of their enhanced charge carrier mobility, minimal trap density,

reduced exciton binding energy of excitons, excellent optical absorption, and prolonged charge carrier lifetime.^{5–7} However, the volatility and thermal instability of organic cations limit their commercial use.^{7–14} Creating more environmentally friendly PSCs requires the innovation of eco-friendly and non-toxic materials.^{14–17} Lead-free perovskites are becoming more popular for their environmental benefits and potential use in electronic devices, especially halide double perovskites, which are ideal for solar and thermoelectric devices.^{18–22} Reproducibility presents another challenge since the performance of PSCs can fluctuate greatly depending on the materials used and fabrication processes.^{23–25} Scaling up production remains difficult as the creation of affordable, efficient, and high-capacity perovskite solar panels poses challenges. To address these issues, we focus on the A_3MX_3 group of inorganic compounds, known for their strong potential in solar energy capture.^{26–30} Several researchers have conducted experimental studies on this inorganic compound from the A_3MX_3 group, publishing their findings in well-regarded journals. Their research emphasizes the unique structural, optical, and electronic properties of the compound. Additionally, these studies investigate its potential applications in diverse fields such as photovoltaics, optoelectronics, and semiconductor technology. The insights

^a Advanced Energy Materials and Solar Cell Research Laboratory, Department of Electrical and Electronic Engineering, Begum Rokeya University, Rangpur 5400, Bangladesh. E-mail: ferdousapee@gmail.com

^b College of Remote Sensing and Geophysics, Al-Karkh University of Science, Al-Karkh Side, Haifa St. Hamada Palace, Baghdad 10011, Iraq. E-mail: mustafa_kareem97@yahoo.com

^c Technology Innovation & Development Foundation, Indian Institute of Technology Guwahati, Guwahati, Assam, 781039, India

^d Department of Chemistry, College of Science, King Khalid University, Abha 61413, P.O. Box 9004, Saudi Arabia

^e Centre for Research Impact & Outcome, Chitkara University Institute of Engineering and Technology, Chitkara University, Rajpura, 140401, Punjab, India

gained contribute to advancements in synthesis, characterization, and performance optimization, fostering further progress in materials science and technological innovation.^{31–35} This article introduces a set of new cubic inorganic compounds, Ba_3MCl_3 (where $\text{M} = \text{Sb, As, P}$ and N), belonging to the lead-free A_3MX_3 group. Studying the previously unexplored mechanical, optoelectronic, and thermodynamic properties of these materials has shown that they could be useful, particularly in optoelectronics and solar cell technology.

The current study employs first-principles computations using DFT^{36,37} to investigate the various characteristics of this material. The SCF method was exploited to analyze the DOS, ECD, and band structure. The CASTEP method, based on DFT, was applied to examine the properties of Ba_3MCl_3 ($\text{M} = \text{N, P, As, and Sb}$).^{38,39} Despite the lack of detailed theoretical work on the optical and electronic characteristics of these perovskite materials in the existing literature, its significant crystal features and practical applications prompted our investigation. We conducted a comprehensive analysis of its physical attributes using DFT simulations with the CASTEP code, comparing the results with similar compounds. Subsequently, investigations were conducted in hybrid PSCs using A_3MX_3 materials with a CdS ETL, focusing on the impact of layer thickness, doping levels, bulk defect density, QE and JV characteristics. Ultimately, the efficiency of all proposed devices under optimal conditions was evaluated. Although it is a set of novel inorganic compounds, Ba_3MCl_3 ($\text{M} = \text{Sb, As, P}$ and N) exhibits promising properties, suggesting its suitability as an effective absorber and for optoelectronic applications due to its excellent electronic and optical characteristics. We anticipate that this study will significantly contribute to research on perovskite-based technologies in modern technology.

2. Experimental

2.1. Computational details

In this study, we conducted first-principles DFT^{40,41} calculations utilizing the CASTEP method⁴² to explore the characteristics of Ba_3MCl_3 ($\text{M} = \text{Sb, As, P}$ and N) perovskite cells. The Kohn–Sham equation⁴³ was employed to ascertain the crystal system. The process began with geometric optimization, followed by electronic property calculations employing ultrasoft pseudopotentials⁴⁴ and the BFGS⁴⁵ algorithm. GGA⁴⁶ and the PBE approach were utilized to improve our understanding of the characteristics of Ba_3MCl_3 perovskite cells ($\text{M} = \text{Sb, As, P}$ and N). For this research, we set specific convergence standards, including an energy cut-off of 700 eV, a highest displacement of 0.0002 Å, a highest force of 0.05 eV per atom, a SCF tolerance of 1.0×10^{-6} eV per atom, and a highest energy of 2.0×10^{-5} eV per atom. For accurate computations, we applied a $7 \times 7 \times 7$ k -point mesh based on the Monkhorst–Pack scheme⁴⁷ for sampling the BZ. The SCF method was exploited to compute the DOS and band structure, while also establishing parameters for the ECD. To examine the optical characteristics, we applied the linear feedback approach to measure how the dielectric function varies with frequency. Additionally, we computed the refractive index, the

conductivity's real and imaginary segments, and the dielectric constant. Convergence checks were carried out to establish the chosen k -point mesh size and convergence criteria, ensuring both accuracy and computational efficiency. These computational approaches were carefully chosen to guarantee the precision and dependability of the results gained. In summary, this computational approach proposes an in-depth examination of the characteristics of Ba_3MCl_3 materials ($\text{M} = \text{Sb, As, P}$ and N) and may serve as a valuable tool in the future.

2.2. Chemical reactions

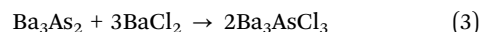
However, the chemical reaction of this inorganic compound Ba_3MCl_3 is outlined below. The Ba_3NCl_3 inorganic compound consisting of barium (Ba), nitrogen (N), and chlorine (Cl), forms through a specific chemical reaction, as shown by eqn (1).⁴⁸



On the other hand, the creation of the inorganic compound Ba_3PCl_3 is given below. This compound, composed of barium (Ba), phosphorus (P), and chlorine (Cl), is produced through a particular chemical reaction, as shown by eqn (2).



Additionally, the synthesis of the inorganic compound Ba_3AsCl_3 is detailed below. This compound, which comprises barium (Ba), arsenic (As), and chlorine (Cl), is formed through a precise chemical reaction, as shown by eqn (3). The process involves the careful combination of these elements in exact proportions, leading to the creation of Ba_3AsCl_3 .



The formation of the inorganic compound Ba_3SbCl_3 is described below. This compound, made up of barium (Ba), antimony (Sb), and chlorine (Cl), is produced through a specific chemical reaction. The procedure requires the precise mixing of these elements in the correct proportions, resulting in the synthesis of Ba_3SbCl_3 as shown by eqn (4).



3. Results and discussion

3.1. Structural study of Ba_3MCl_3 ($\text{M} = \text{N, P, As, and Sb}$)

Fig. 1(a) shows that the crystal structures of Ba_3MCl_3 ($\text{M} = \text{N, P, As, and Sb}$) belong to the cubic space group $Pm\bar{3}m$ (no. 221). Each structure comprises a unit cell containing 7 atoms. The Cl atoms hold the 3d Wyckoff site with relevant positions of (0, 0, 0.5) on the borders of one face, while the central position is occupied by the M atom (N, P, As, and Sb) at the 1b Wyckoff site with relevant positions of (0.5, 0.5, 0.5). Additionally, the Ba atoms at the 3c Wyckoff site are located near the vertices of a single cell, with relative positions of (0.5, 0.5, 0). Fig. 1(b) visually signifies the trajectory in k -space within the primary BZ. The electronic band arrangement of Ba_3MCl_3 is determined

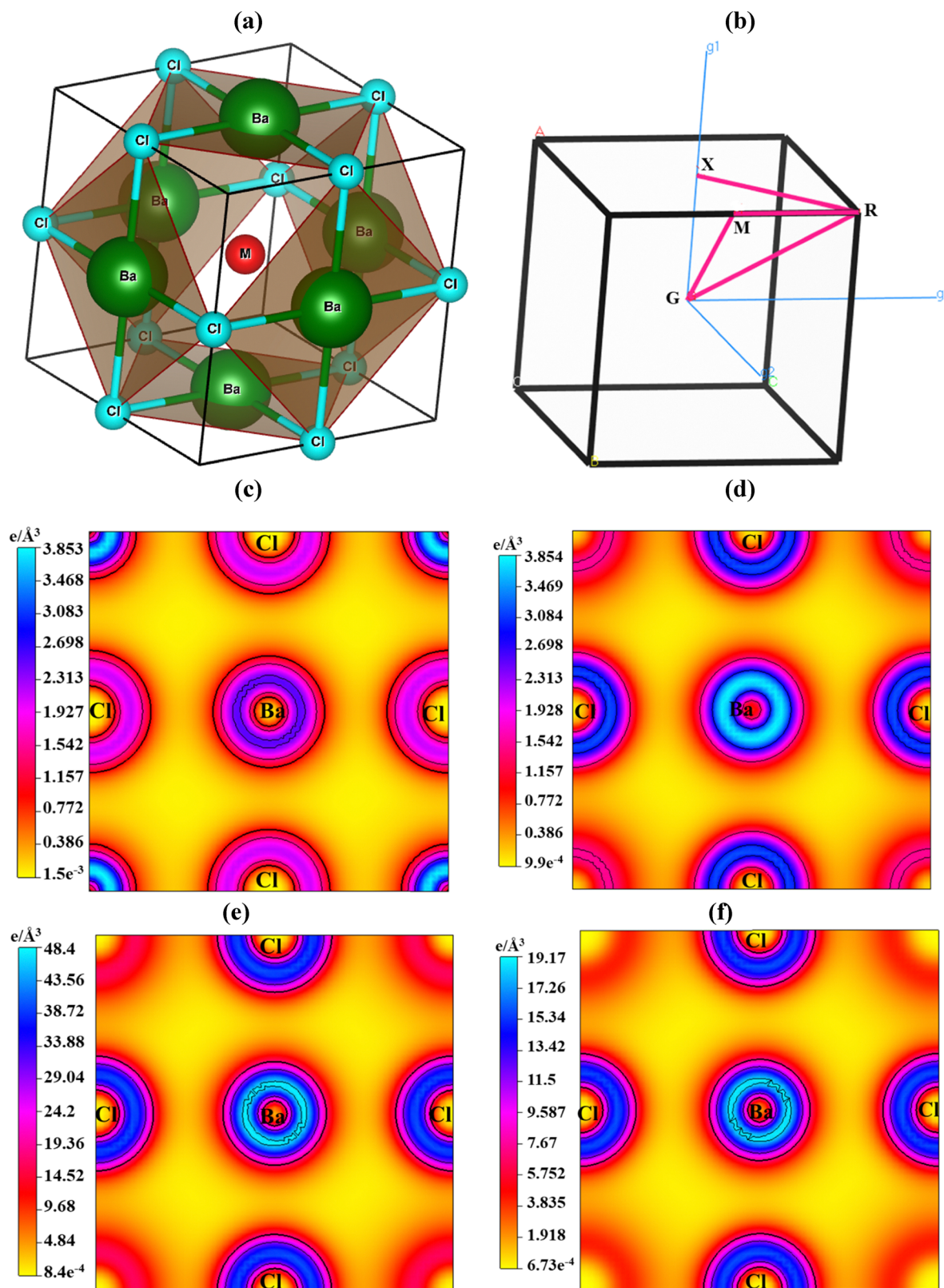


Fig. 1 (a) Crystal structure of Ba_3MCl_3 ($\text{M} = \text{N}, \text{P}, \text{As}, \text{and Sb}$), (b) BZ path (X-R-M-G-R) and the distribution of electronic charges in (c) Ba_3NCl_3 , (d) Ba_3PCl_3 , (e) Ba_3AsCl_3 and (f) Ba_3SbCl_3 .

by the points of high symmetry (X-R-M-G-R) in the BZ, where the band diagram is replicated throughout the structure.

The most optimized structures of Ba_3NCl_3 , Ba_3PCl_3 , Ba_3AsCl_3 , and Ba_3SbCl_3 yielded the computed lattice parameters of 6.14,

6.44, 6.51, and 6.69, respectively. The respective unit cell volumes of Ba_3NCl_3 , Ba_3PCl_3 , Ba_3AsCl_3 , and Ba_3SbCl_3 are 1563.6448 (a.u.)³, 1804.2245 (a.u.)³, 1863.6998 (a.u.)³, and 2022.6062 (a.u.)³.

3.2. Electron charge density

The type of bonding present among different atoms is elucidated by means of the arrangement of charge density. To understand the movement of the charge between atoms and discern the bonding within Ba_3MCl_3 ($\text{M} = \text{Sb, As, P and N}$), we evaluated the charge density. Fig. 1(c)–(f) illustrate the pattern of electrical charge density in Ba_3MCl_3 ($\text{M} = \text{Sb, As, P and N}$), respectively. The images feature a scale bar positioned on the left side that utilizes color representation to indicate the electron density's intensity. The cyan color corresponds to regions of high electron density, whereas the yellow color indicates areas with low electron density. In this case, the ECD is highest around the Cl ion and lowest around the Ba ion. Because an ionic bond develops when negative and positive charges are balanced at atomic locations, the absence of overlap between the Ba and Cl ions means an ionic bond. In contrast, the charge density is comparable between Cl and M ions (where $\text{M} = \text{N, P, As, and Sb}$), which is indicative of a covalent bond. Additionally, a notable difference in electron density between the Ba and M (N, P, As, and Sb) ions suggests an ionic bond connecting them.

3.3. Electronic study of Ba_3MCl_3 ($\text{M} = \text{N, P, As, and Sb}$)

The electrical band arrangement of a material is crucial for understanding its physical features such as charge transport behavior and optical characteristics. In the case of Ba_3MCl_3 ($\text{M} = \text{N, P, As, and Sb}$), its band structures are depicted in Fig. 2 along the BZ path X–R–M–G–R, by employing the PBE process. The analysis reveals band gaps of 0.551 eV, 0.927 eV, 0.980 eV, and 0.996 eV for Ba_3NCl_3 , Ba_3PCl_3 , Ba_3AsCl_3 and Ba_3SbCl_3 , respectively, using the GGA-PBE function at the G point, known for its accuracy.⁴⁹ Notably, different exchange–correlation (XC) functions may yield varying band-gap results.

In this representation, the Fermi level (E_F) is denoted at 0 eV, while the energy stages vary from –6 to +6 eV. The upper lines in the band structure correspond to the CB, whereas those at the Fermi level signify the VB. This direct bandgap emerges from the intriguing alignment of the maximum VB energy state with the minimum CB energy state at the G symmetry point.⁵⁰

The narrow band gap of Ba_3MCl_3 ($\text{M} = \text{N, P, As, and Sb}$) allows efficient capture of visible light and reduces thermalization losses, improving its efficacy in converting light to electricity. Such materials exhibit elevated electron mobility and are proficient in light emission, making them desirable for electronic and optical devices.^{51,52} A smaller band gap permits light absorption with lower energy levels, such as near-infrared wavelengths corresponding to 0.551 eV, 0.927 eV, 0.980 eV, and 0.996 eV band gaps. This analysis suggests the suitability of the material for optoelectronic devices, given its semiconducting nature, which is a crucial consideration for solar cell applications.

In Fig. 2(e)–(h), using the HSE06 functional, the materials Ba_3NCl_3 , Ba_3PCl_3 , Ba_3AsCl_3 and Ba_3SbCl_3 were found to have

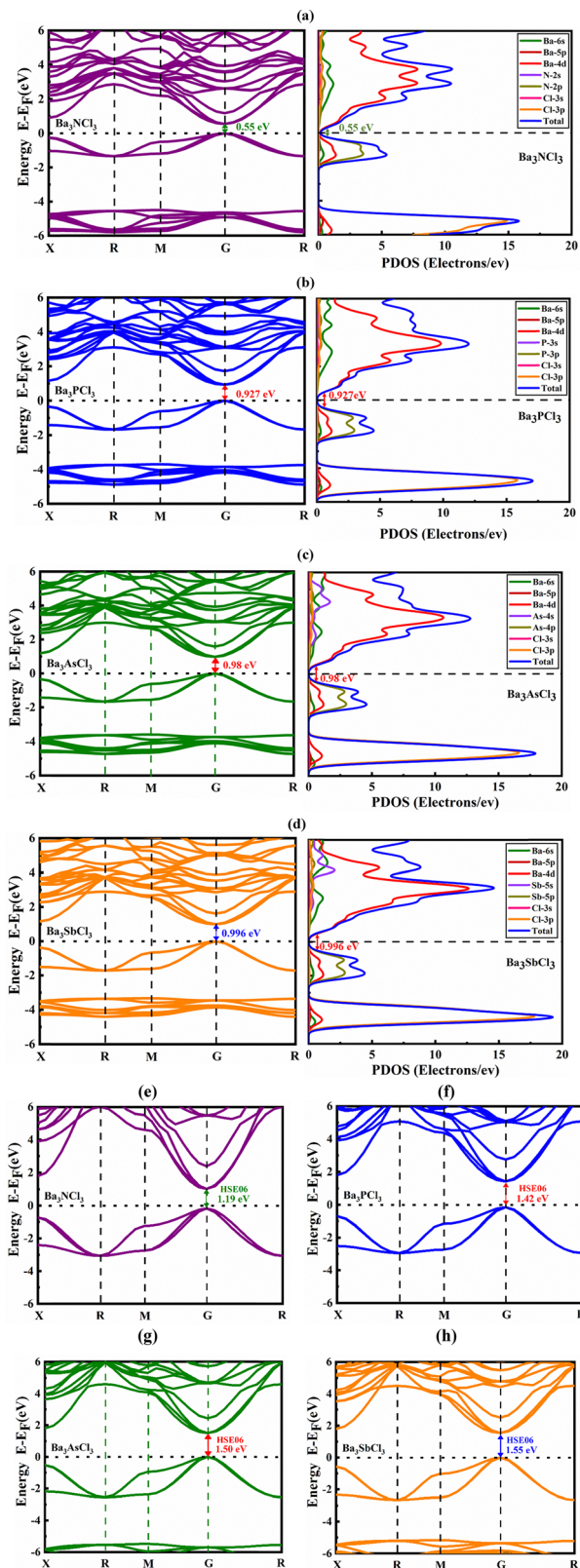


Fig. 2 Electronic band structures and inorganic cubic PDOS structures of (a) Ba_3NCl_3 , (b) Ba_3PCl_3 , (c) Ba_3AsCl_3 , and (d) Ba_3SbCl_3 structures and (e)–(h) the band structures using the HSE06 function.

direct bandgaps of approximately 1.19 eV, 1.42 eV, 1.50 eV, and 1.55 eV, respectively. These values were calculated using the

HSE06 exchange–correlation functional. The band structure analysis, conducted along the trajectory in reciprocal space

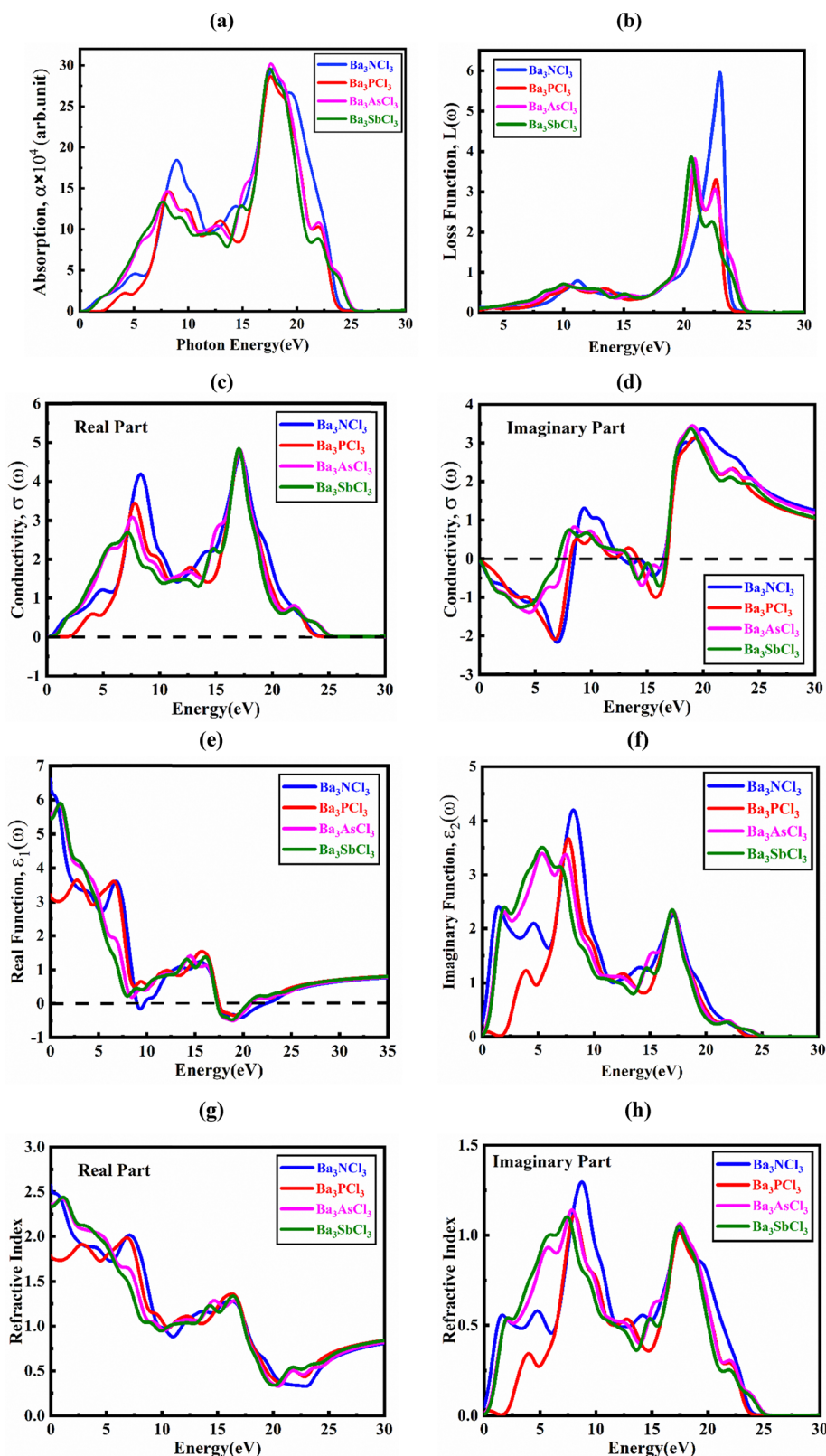


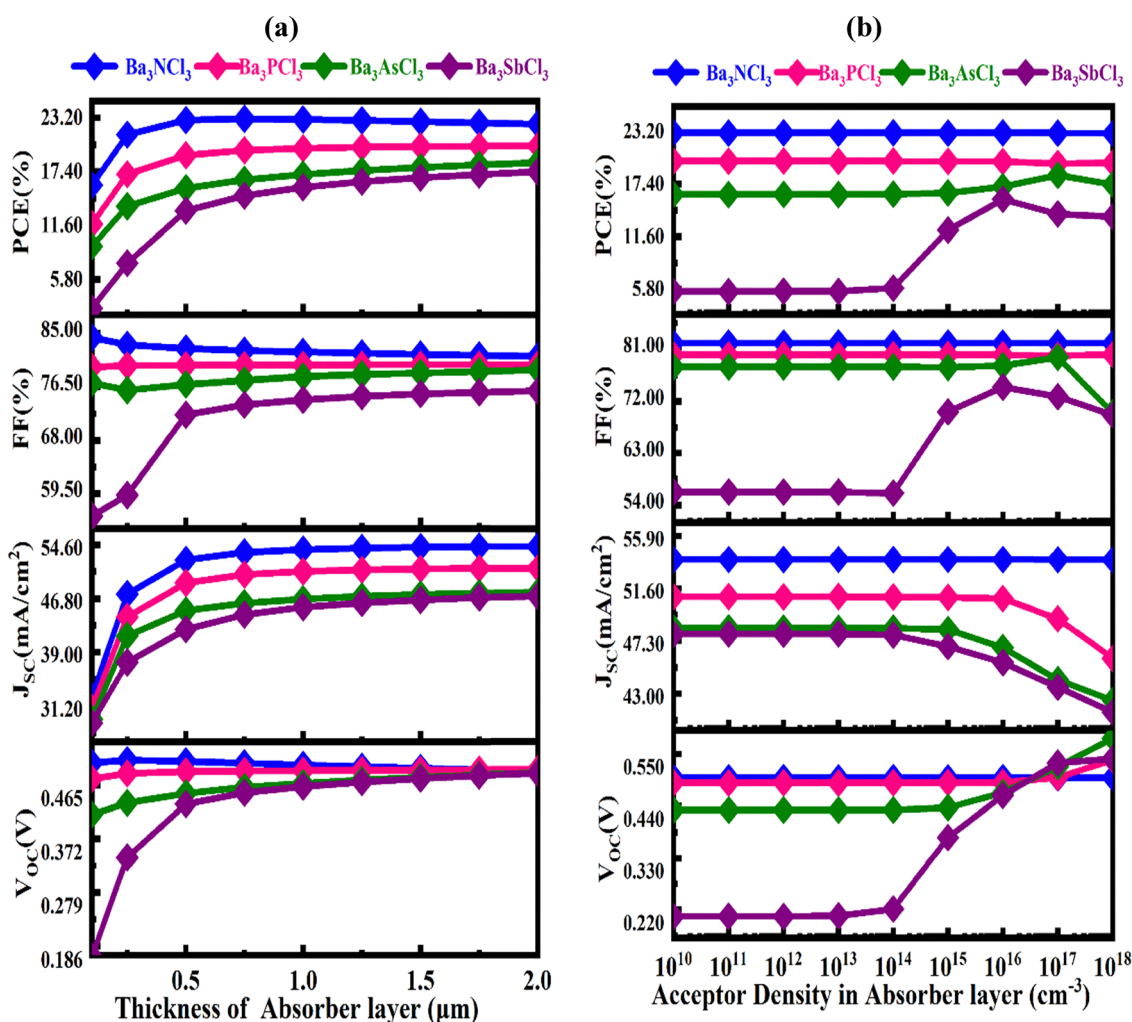
Fig. 3 Energy-associated (a) absorption index, (b) loss function, (c) real, (d) imaginary component of conductivity, (e) real, (f) imaginary dielectric function, (g) real and (h) imaginary segment of refractive index of Ba_3MCl_3 ($\text{M} = \text{N}, \text{P}, \text{As}, \text{and Sb}$).

Table 1 Parameters set for the FTO, ETL, and absorber layer

Parameters	Ba ₃ NCl ₃	Ba ₃ PbCl ₃	Ba ₃ AsCl ₃	Ba ₃ SbCl ₃	CdS	FTO
Thickness (nm)	1000	1000	1000	1000	50	50
Band gap, E_g (eV)	0.55	0.927	0.98	0.996	2.4	3.6
Electron affinity, χ (eV)	3.687	4.5	4.562	4.805	4.4	4.5
Dielectric permittivity (relative), ϵ_r	6.606	3.206	5.602	5.48	9	10
CB effective density of states, N_C (1 cm ⁻³)	6.78×10^{18}	7.728×10^{18}	7.94×10^{18}	9.347×10^{18}	1.8×10^{19}	2×10^{18}
VB effective density of states, N_V (1 cm ⁻³)	1.007×10^{19}	1.09×10^{19}	1.136×10^{19}	1.2×10^{19}	2.4×10^{18}	1.8×10^{19}
Electron mobility, μ_n (cm ² V ⁻¹ s ⁻¹)	60	70	65	45	100	100
Hole mobility, μ_h (cm ² V ⁻¹ s ⁻¹)	55	60	45	40	25	20
N_A (1 cm ⁻³)	1×10^{16}	1×10^{16}	1×10^{16}	1×10^{16}	0	0
N_D (1 cm ⁻³)	0	0	0	0	1×10^{15}	1×10^{18}
Defect density, N_t (1 cm ⁻³)	1×10^{12}	1×10^{12}	1×10^{12}	1×10^{12}	1×10^{12}	1×10^{12}

Table 2 Input parameters of the interface of the Ba₃MCl₃ (M = N, P, As, and Sb) based solar cells

Parameters	Ba ₃ NCl ₃ /SnS ₂	Ba ₃ PbCl ₃ /SnS ₂	Ba ₃ AsCl ₃ /SnS ₂	Ba ₃ SbCl ₃ /SnS ₂
Defect type	Neutral	Neutral	Neutral	Neutral
σ_c (cm ²)	1×10^{-19}	1×10^{-19}	1×10^{-19}	1×10^{-19}
σ_h (cm ²)	1×10^{-19}	1×10^{-19}	1×10^{-19}	1×10^{-19}
E_r	0.6	0.6	0.6	0.6
Total defect density (cm ⁻¹)	10^{12}	10^{12}	10^{12}	10^{12}

**Fig. 4** Influence of alteration of the absorber layer (Ba₃NCl₃, Ba₃PbCl₃, Ba₃AsCl₃ and Ba₃SbCl₃) (a) thickness and (b) acceptor density with PV factors of V_{oc} , J_{sc} , FF and PCE.

(X_R_M_G_R), corresponds to the cubic arrangement of Ba_3MCl_3 under the HSE06 functional.

Typically, PDOS analysis reveals the impact of several atoms and their locations on the band gap of Ba_3MCl_3 compounds. Fig. 2(a)–(d) illustrate the PDOS distribution for Ba_3MCl_3 structures ($\text{M} = \text{Sb, As, P}$ and N) spanning the energy range from -6 to $+6$ eV. The states associated with the Ba and Sb, As, P and N atoms, which interact with Cl in Ba_3MCl_3 ($\text{M} = \text{Sb, As, P}$ and N), are found to spread throughout the total energy spectrum without impacting the band gap. This proposal proposes that the bonding between Ba–Cl, N–Cl, P–Cl, As–Cl, and Sb–Cl is predominantly covalent in nature. Furthermore, in Ba_3NCl_3 , Ba_3PCl_3 , Ba_3AsCl_3 , and Ba_3SbCl_3 , electron charge transfer occurs

from Ba and N, P, As, and Sb to Cl, respectively, potentially resulting in substantial changes in atomic situations. Because of their separation from the Fermi level, the Ba^{2+} atoms have only a minimal influence on the determination of band edge conditions in this scenario. In our study of the cubic phase, we noted that the VB of Ba_3MCl_3 is mainly shaped by the Cl-3p orbital, whereas the CB is mainly determined by the Ba-4d orbital, with slight involvement from the N-2s, P-3s, As-4s and Sb-5s orbitals. The strong contribution from Cl-3p orbitals in the valence band indicates a significant ionic character in the bonding between Cl and Ba. The Ba-4d orbitals' involvement in the conduction band suggests that these states are important for electronic transitions and charge carrier transport. This combination of contributions from both orbitals plays a critical role in defining the material's bandgap and electronic structure.

3.4. Optical study of Ba_3MCl_3 ($\text{M} = \text{N, P, As, and Sb}$)

Various applications, including optical coatings, rectifiers, light absorbers, and devices converting light into electricity, are explored depending on their optical characteristics. When subjected to an external electromagnetic wave, a material's interaction with photons can reveal facts about its characteristics and

Table 3 Performance metrics of solar cells using the CdS ETL are evaluated against various absorbers

Parameters	Ba_3NCl_3	Ba_3PCl_3	Ba_3AsCl_3	Ba_3SbCl_3
V_{OC} (V)	0.5	0.49	0.47	0.46
J_{SC} (mA cm^{-2})	53.97	50.78	46.76	45.55
FF (%)	82.06	80.01	78.15	74.49
PCE (%)	23.06	19.93	17.12	15.71

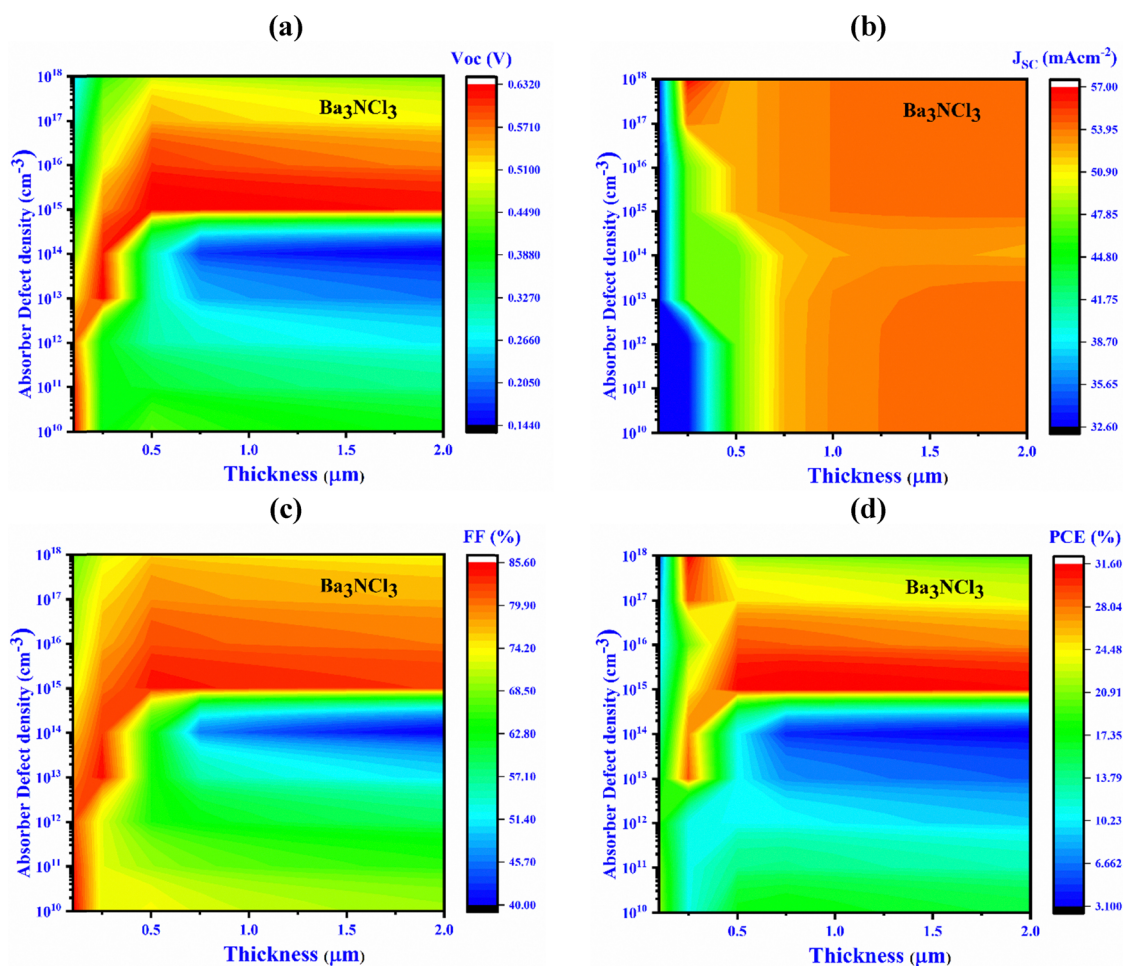


Fig. 5 Influence of variations in absorber thickness and defect density (device-I, Ba_3NCl_3) on key PV performance factors: (a) V_{OC} , (b) J_{SC} , (c) FF, and (d) PCE.

potential applications relative to energy. An investigation of electronic conversions between bond types, occupied and unoccupied energy states, band arrangements, and internal structural properties of compounds is achieved by examination of their optical spectra.⁵³ Certain optical properties of a perovskite that vary with energy levels comprise energy loss function $L(\omega)$, reflectivity $R(\omega)$, optical conductivity $\sigma(\omega)$, refractive index $N(\omega)$, dielectric function $\varepsilon(\omega)$, and absorption coefficient $\alpha(\omega)$. We compute and examine these optical features to explore how Ba_3MCl_3 ($M = \text{N}, \text{P}, \text{As}, \text{and Sb}$) reacts to incoming photons in this section.

Fig. 3(a)–(h) illustrate the spectra for the parameters mentioned above, spanning incident energies equal to 40 eV and an exclusively polarized electric field that has the crystal plane $[1\ 0\ 0]$.⁵⁴ The complex dielectric constant, which changes with frequency or energy, is attained through the Kramers–Kronig transformation as follows:⁵⁵

$$\varepsilon(\omega) = \varepsilon_1(\omega) + i\varepsilon_2(\omega) \quad (5)$$

Furthermore, other optical properties were determined using the real portion $\varepsilon_1(\omega)$ and the imaginary portion $i\varepsilon_2(\omega)$.

Fig. 3(a) illustrates the optical absorption coefficient of Ba_3MCl_3 ($M = \text{N}, \text{P}, \text{As}, \text{and Sb}$).⁵⁴ The optical absorption coefficient plays a vital role in evaluating a material's ability to absorb light, providing valuable insights into its suitability for efficient solar energy conversion.^{56,57} The absorption coefficient spans from 5 to 25 eV, with the absorption being notably high, reaching its peak around 17 eV of photon energy for all materials. It starts at 0.7 eV and diminishes to zero after 25 eV, indicating a considerable photon energy absorption ranging from 0.7 to 25 eV. This proposes that Ba_3MCl_3 possesses a wider optical bandgap, resulting in significant photon absorption at high energies.

Fig. 3(b) depicts the loss function $L(\omega)$, which varies with energy or frequency. This component, typically imaginary, within the dielectric function mimics the way light is absorbed by a semiconductor. The peak is observed at a photon energy level of 23 eV for Ba_3NCl_3 and 21 eV for the other three materials, after which it returns to zero. This peak indicates the plasmon energy characteristic of the respective materials. The plasma oscillates at this exact energy due to the collective motions of charged particles. Note that significant decreases in the reflectivity and absorption coefficient coincide with the plasma energy.

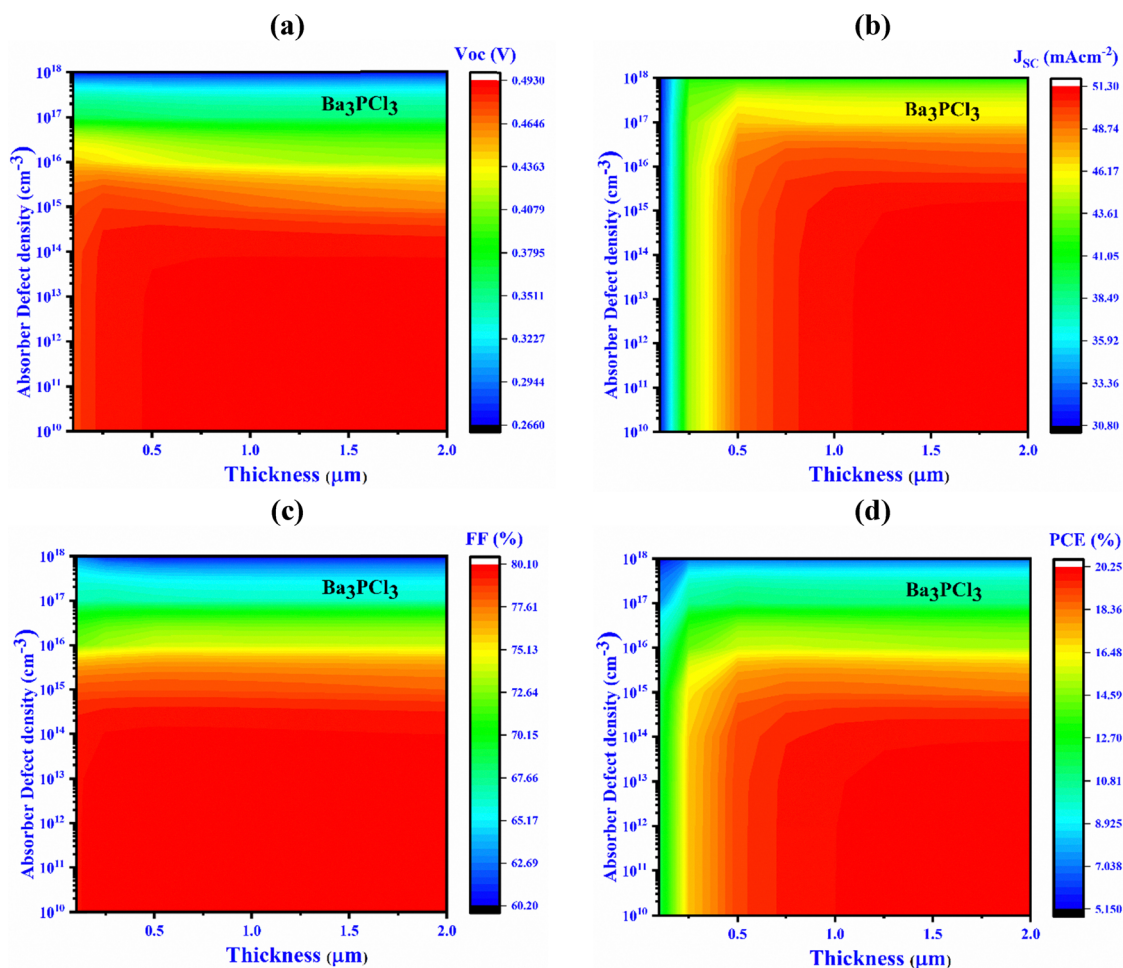


Fig. 6 Influence of variations in absorber thickness and defect density (device II, Ba_3PbCl_3) on key PV performance factors: (a) V_{OC} , (b) J_{SC} , (c) FF, and (d) PCE.

Fig. 3(c) and (d) display the optical conductivity's real and imaginary parts for Ba_3MCl_3 ($\text{M} = \text{N}, \text{P}, \text{As}, \text{and Sb}$). The imaginary part of the photoconductivity initiates at 0.42 eV, while the real portion begins with approximately 0 eV for all materials, affirming the material's favorable photoconductivity characteristics. Furthermore, the real part drops to zero beyond 25 eV of photon energy, suggesting an improvement in the conductivity at upper energies.⁵⁸ This phenomenon could be attributed to the movement of electrons to elevated energy states, enabling their participation in electrical flow.

Fig. 3(e) and (f) depict the dielectric function's real $\varepsilon_1(\omega)$ and imaginary portion $\varepsilon_2(\omega)$ for Ba_3MCl_3 ($\text{M} = \text{Sb}, \text{As}, \text{P}$ and N). These components are derived from the elements of the momentum matrix, considering all feasible conversions between the filled and empty electronic conditions.^{59,60} The real segment of the dielectric function, $\varepsilon_1(\omega)$, corresponds to electrical polarization, while the imaginary component, $\varepsilon_2(\omega)$, relates to dielectric loss.^{61,62} Notably, the real portion reaches zero at 9 eV photon energy for Ba_3NCl_3 and 17 eV for the other three materials and gradually approaches unity. In contrast, the

imaginary part $\varepsilon_2(\omega)$ begins at zero and drops back to zero when the photon energy hits 25 eV. The dielectric constant of Ba_3MCl_3 indicates metallic properties depending on its band structure and electronic DOS, also showing semiconducting characteristics and high reflectivity.⁶¹

In Fig. 3(g) and (h), a complex factor, the refractive index, is depicted. It is also a function dependent on energy or frequency and can be formulated as:⁵⁵

$$N(\omega) = n(\omega) + ik(\omega) \quad (6)$$

where the extinction factor is indicated by $k(\omega)$, representing the imaginary portion of $N(\omega)$. The refractive index's imaginary portion (extinction factor) gauges the absorption of electromagnetic radiation by the materials, while the real part resolves the phase velocity in the materials.⁶³ It can be observed that the refractive index's real part demonstrates a greater value in the visible spectrum at low phonon-energy levels. Thus, the material under investigation demonstrates optical features appropriate for application in optoelectronic devices.⁶⁴

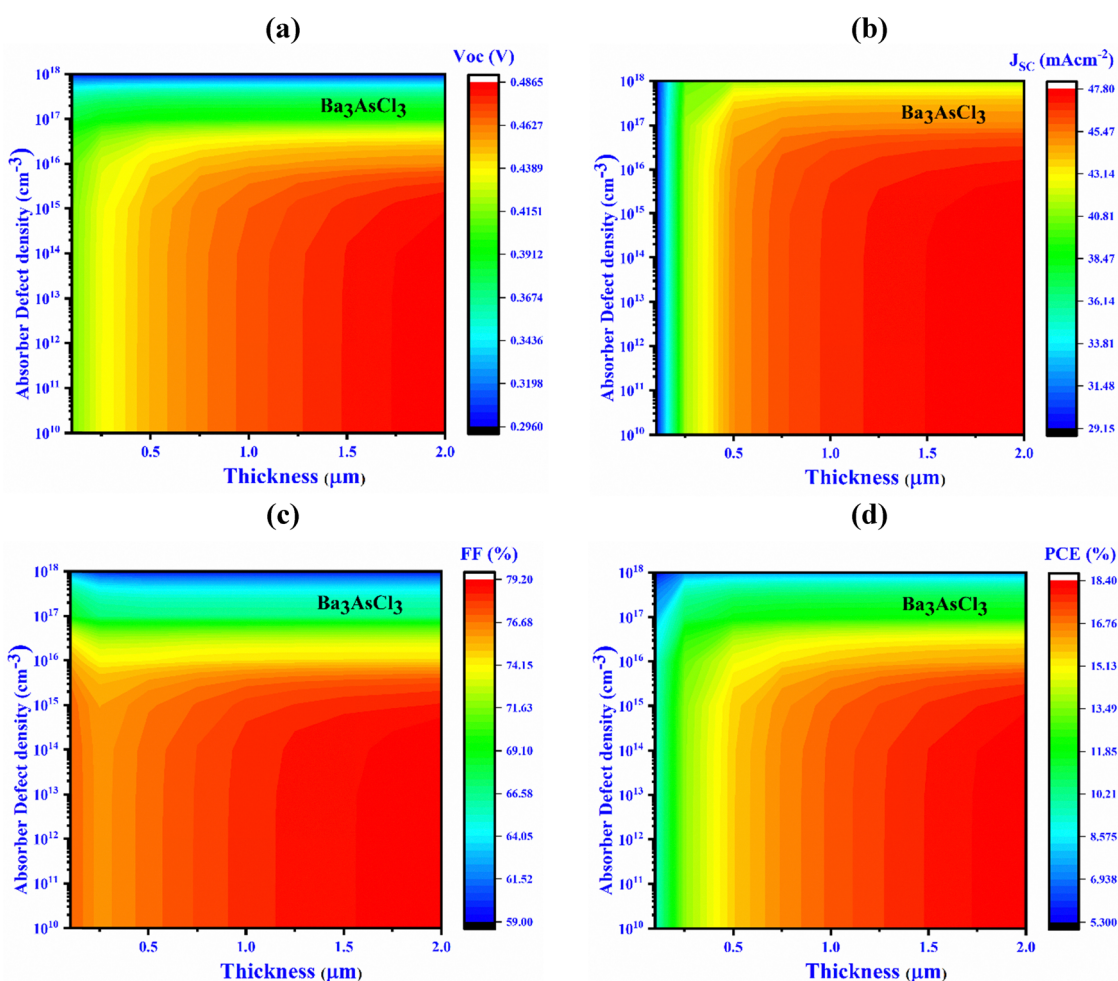


Fig. 7 Influence of variations in absorber thickness and defect density (device-III, Ba_3AsCl_3) on key PV performance parameters: (a) V_{OC} , (b) J_{SC} , (c) FF, and (d) PCE.

3.5. Design of devices and simulation techniques

The proposed photovoltaic cell structure, represented as Al/FTO/CdS/(Ba₃NCl₃/Ba₃PCl₃/Ba₃AsCl₃/Ba₃SbCl₃)/Au, includes devices labeled device-I (Ba₃NCl₃), II (Ba₃PCl₃), III (Ba₃AsCl₃), and IV (Ba₃SbCl₃). These devices have been simulated utilizing the SCAPS-1D software. The essential formulas were resolved to thoroughly analyze and predict the electrostatic potential formulas in steady-state situations, as well as the electron-hole continuity formulas for both structures.⁶⁵ The solar cell contains a p-type absorber layer (Ba₃NCl₃/Ba₃PCl₃/Ba₃AsCl₃/Ba₃SbCl₃), a highly n-doped ETL made of CdS and an FTO window stratum. The metal electrodes at the front and rear are aluminum (Al) and gold (Au), with WF of 4.2 eV (100) and 5.37 eV (110), respectively. The distinct alignment of the quasi-Fermi levels F_n and F_p under illumination provides evidence for the formation of electron and hole pairs inside the device. The electric fields and intrinsic potential at the absorber/ETL interface facilitate the separation of light-induced electron-hole pairs. The imitation data for the active materials FTO, CdS, Ba₃NCl₃, Ba₃PCl₃, Ba₃AsCl₃, and Ba₃SbCl₃, presented in Table 1, were derived from the established literature and the DFT calculations of this study,

with the electron and hole paces set at 10^7 cm s^{-1} .^{66,67} The specifications for each of the four proposed PV devices at the absorber/ETL boundary are detailed in Table 2.

3.6. Optimization of absorber layer thickness and charge carrier concentration

Fig. 4(a) displays the impact of altering the absorber layer thickness at 100–2000 nm to achieve optimal outcomes in the suggested devices without altering other factors, as shown in the previous table. It was observed that both carrier generation and recombination speeds rise significantly with a thicker absorber layer. A thickening of the absorber layer led to an upsurge in the V_{OC} of the PSCs in every configuration. The maximum V_{OC} of 0.5 V was attained for device I. Similarly, improvements in V_{OC} were observed for device II (from 0.47 to 0.49 V), device III (from 0.42 to 0.49 V), and device IV (from 0.17 to 0.49 V). The J_{SC} also increased with the denser absorber layer, mainly because of improved absorption across the spectrum, with a focus on longer wavelengths. J_{SC} values rose from 32.61 to 54.45 mA cm^{-2} in device I, 30.99 to 51.26 mA cm^{-2} in device II, 29.32 to 47.78 mA cm^{-2} in device III, and 28.79 to 47.19 mA cm^{-2} in device IV. The rise in J_{SC} can be ascribed to

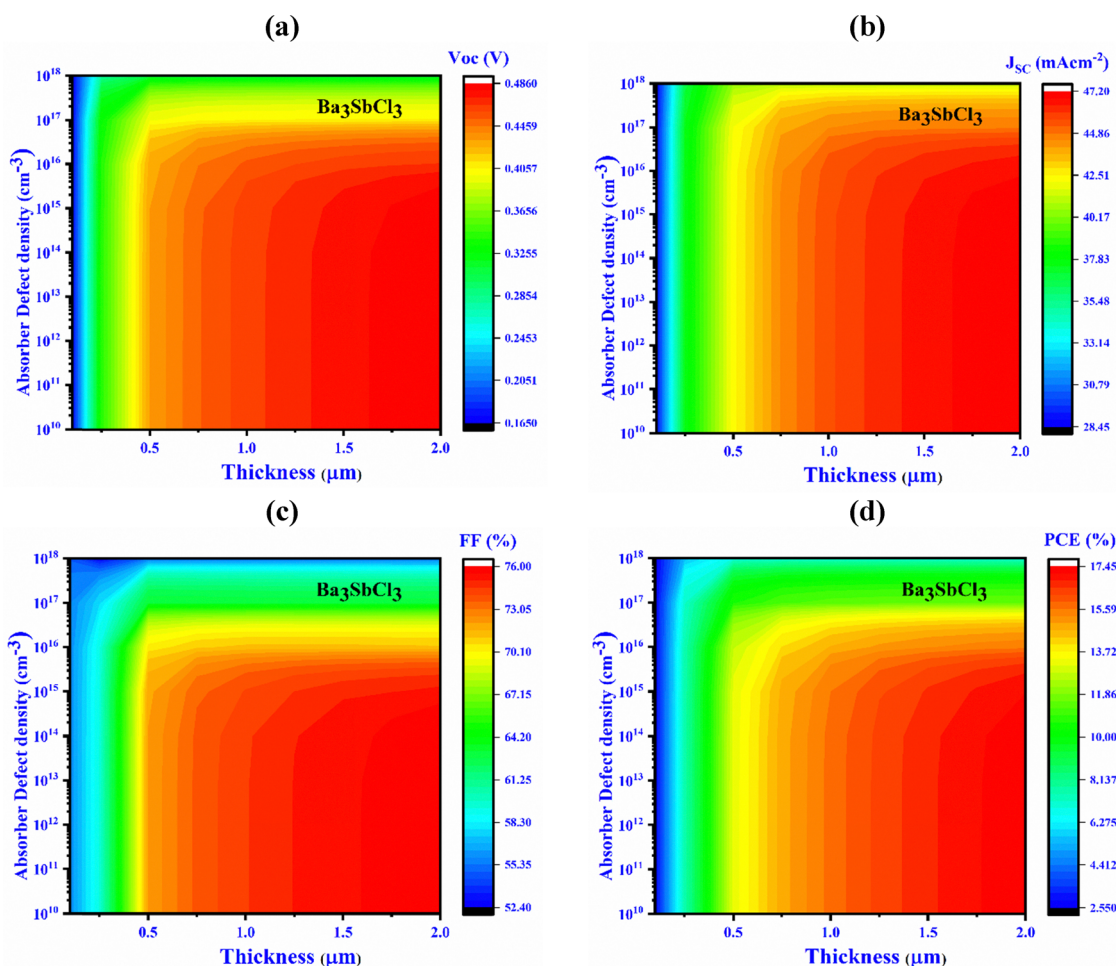


Fig. 8 Influence of variations in absorber thickness and defect density (device-IV, Ba₃SbCl₃) on key PV performance parameters: (a) V_{OC} , (b) J_{SC} , (c) FF, and (d) PCE.

the greater formation of electron and hole pairs from increased photon absorption in a thicker absorber. These changes in V_{OC} and J_{SC} are in line with findings described in previous studies.^{68–70}

FF values improved from 79.64% to 80.05% for device II, from 76.03% to 79.19% for device III, and from 55.97% to 75.92% for device IV with increasing absorber thickness, but FF values improved from 81.37% to 84.39% for device I with decreasing absorber thickness. PSCs generally operate most efficiently once the absorber thickness corresponds to the charge carriers' diffusion length. Although thicker absorber layers result in higher photon absorption, they also lead to increased recombination rates. Thus, optimizing between these factors is essential for achieving high-efficiency PSCs.^{71–73}

Fig. 4(b) shows how electrical properties, such as J_{SC} , PCE, V_{OC} and FF, vary with acceptor doping density (N_A) ranging from 10^{10} to 10^{18} cm⁻³ for the absorbers Ba₃NCl₃, Ba₃PbCl₃, Ba₃AsCl₃ and Ba₃SbCl₃ in the proposed configuration. During optimization, the V_{OC} of the PSCs exhibited minimal variation up to an N_A of 10^{14} cm⁻³.⁷⁴ The maximum V_{OC} observed was 0.5 V for device I (mainly constant all the time), 0.54 V for device II, 0.58 V for device III and 0.54 V for device IV (which

showed a relatively higher rate of change). The fill factor exhibited similar trends, with a noticeable 4–5% improvement, reaching nearly saturated values of 82.06%, 80.01%, 78.15%, and 74.49% for Ba₃NCl₃, Ba₃PbCl₃, Ba₃AsCl₃ and Ba₃SbCl₃, respectively, at an N_A of 10^{16} cm⁻³, as shown in Table 3. This behavior aligns with previous reports.^{75,76} However, when the acceptor density in the absorber layer was varied from 10^{10} to 10^{15} cm⁻³, the J_{SC} remained almost constant. Beyond 10^{15} cm⁻³, the J_{SC} marginally decreased for Ba₃PbCl₃, Ba₃AsCl₃ and Ba₃SbCl₃. For Ba₃NCl₃, the J_{SC} remained unchanged up to 10^{18} .

3.7. Impact of device thickness (I, II, III, and IV) and defect density

Fig. 5 displays the impact of the defect density (N_t) on the efficiency of PV cells by illustrating the alterations in both the thickness and the N_t of the Ba₃NCl₃ absorber layer, varying from 0.1 to 2.0 μ m and from 10^{10} to 10^{18} cm⁻³, respectively. The solar cell outcome noticeably deteriorates when the N_t of Ba₃NCl₃ surpasses 10^{12} cm⁻³.⁶⁸ J_{SC} , V_{OC} , PCE and FF for Al/FTO/CdS/Ba₃NCl₃/Au structures drop from 57 to 32.6 mA cm⁻², from 0.63 to 0.14 V, from 31.6% to 3.1%, and from 85.6% to 40%, respectively. As shown in Fig. 5(a), a peak V_{OC} of 0.5 V is

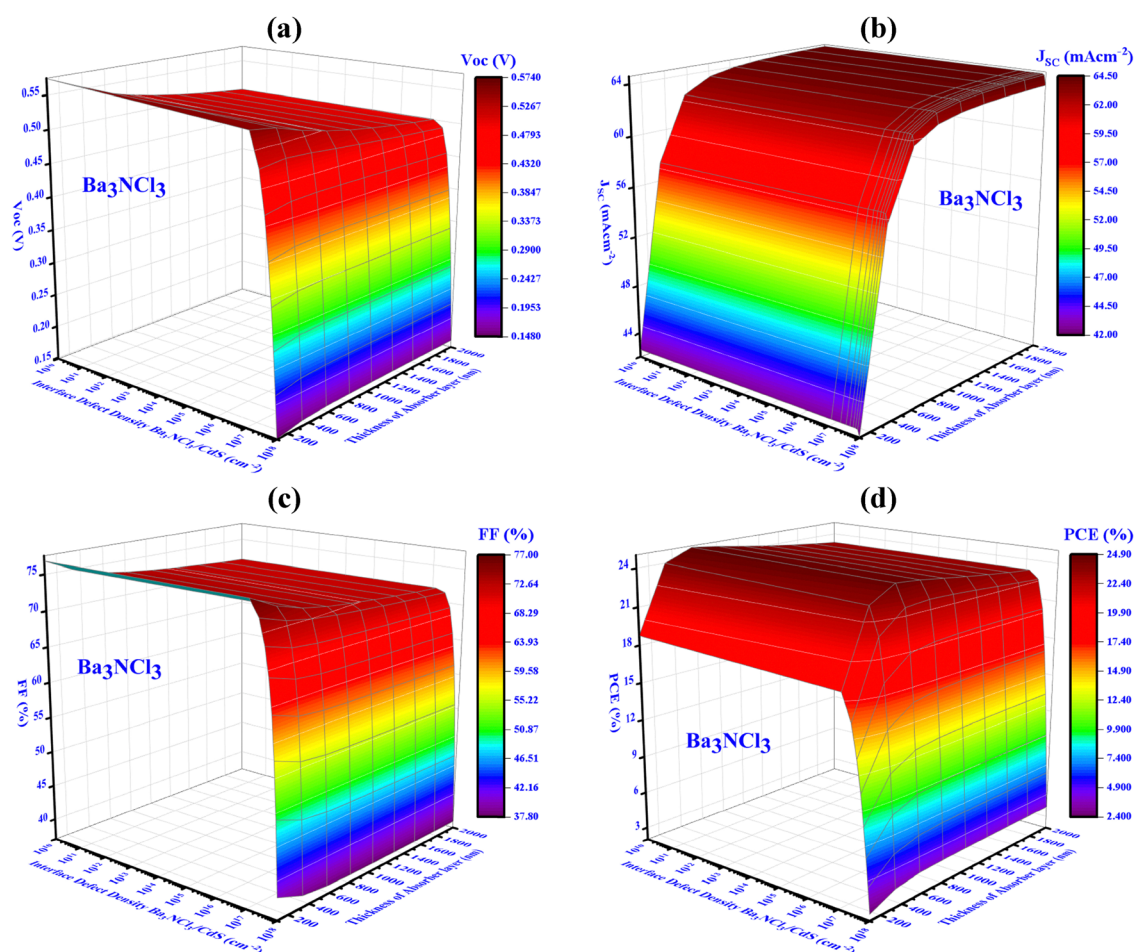


Fig. 9 Influence of variations in absorber thickness and defect interface density (device-I, Ba₃NCl₃) on key PV performance factors: (a) V_{OC} , (b) J_{SC} , (c) FF, and (d) PCE.

obtained if the N_t is kept underneath 10^{12} cm^{-3} and the thickness remains less than $1 \mu\text{m}$. In contrast, if the N_t goes beyond 10^{12} cm^{-3} , the V_{OC} decreases markedly to 0.16 V .

Fig. 5(b) and (c) indicate that to attain the highest values of J_{SC} and FF of 53.97 mA cm^{-2} and 82.06% , respectively, the thickness should exceed $1 \mu\text{m}$ and the N_t should remain below 10^{12} cm^{-3} . Fig. 5(d) depicts that the highest conversion efficiency, exceeding 23.06% , is obtained once the thickness is within 0.1 to $2.0 \mu\text{m}$ and the N_t is up to 10^{12} cm^{-3} . Higher carrier recombination rates, caused by increased defects in the absorber layer, consequently reduce the cell's efficiency.^{77–79} The optimal criteria for reaching a maximum PCE of 23.06% for device-I have been identified. This involves ensuring an absorber layer thickness of $1.0 \mu\text{m}$ for Ba_3NCl_3 with a N_t of 10^{12} cm^{-3} . With these parameters, the PV cell obtained a V_{OC} of 0.5 V , a J_{SC} of 53.97 mA cm^{-2} , and an FF of 82.06% .

For $\text{Al/FTO/CdS/Ba}_3\text{PbCl}_3/\text{Au}$ (device II) structures, increasing the defect density leads to a decline in J_{SC} , PCE, V_{OC} , and FF, while thickening the absorber layer improves these values. In particular, these parameters increase significantly with a thickness up to $1 \mu\text{m}$, beyond which further increases produce only marginal improvements. In contrast, the values drop sharply as the N_t increases up to 10^{12} cm^{-3} , and any increase

beyond this threshold results in a slight decline. Therefore, the optimal absorber layer thickness is $1 \mu\text{m}$ with a N_t of 10^{12} cm^{-3} . In these optimal circumstances, J_{SC} , V_{OC} , PCE, and FF reach values of 50.78 mA cm^{-2} , 0.49 V , 19.93% , and 80.01% , respectively. Fig. 6(a) shows that the highest V_{OC} of 0.49 V is gained with a thickness less than $1 \mu\text{m}$ and a N_t below 10^{12} cm^{-3} . However, exceeding this defect density threshold significantly reduces the V_{OC} to 0.27 V . Fig. 6(b) and (c) suggest that to achieve the highest J_{SC} and FF values of 50.78 mA cm^{-2} and 80.01% , the thickness should exceed $1 \mu\text{m}$ and the N_t should remain below 10^{12} cm^{-3} . Fig. 6(d) specifies that maintaining a thickness between 0.1 and $2.0 \mu\text{m}$ and a N_t equal to 10^{12} cm^{-3} yields the peak conversion efficiency, surpassing 19.93% .

The FF, J_{SC} , PCE, and V_{OC} of the $\text{Al/FTO/CdS/Ba}_3\text{AsCl}_3/\text{Au}$ (device III) structures decline significantly from 79.2% to 59% , 47.8 to 29.15 mA cm^{-2} , 18.4% to 5.3% , and 0.49 to 0.3 V , respectively. Fig. 7(a) shows that the peak V_{OC} of 0.47 V is reached when the N_t is underneath 10^{12} cm^{-3} and the absorber layer thickness is under $1 \mu\text{m}$. When N_t exceeds 10^{12} cm^{-3} , V_{OC} drops sharply to 0.31 V . Fig. 7(b) and (c) suggest that to obtain the highest values of J_{SC} and FF of 46.76 mA cm^{-2} and 78.15% , the thickness needs to exceed $1 \mu\text{m}$ and the N_t should

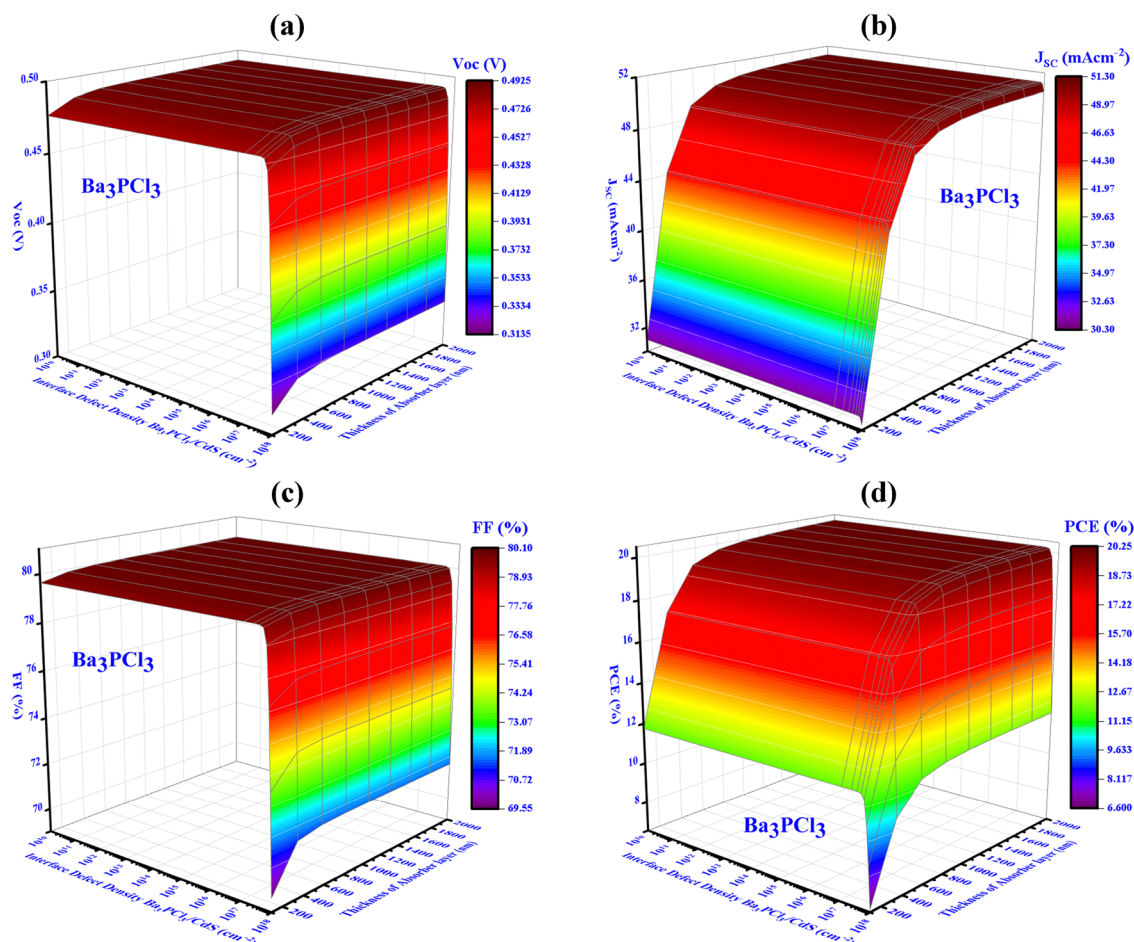


Fig. 10 Influence of variations in absorber thickness and defect interface density (device-II, Ba_3PbCl_3) on key PV performance factors: (a) V_{OC} , (b) J_{SC} , (c) FF, and (d) PCE.

remain under 10^{12} cm^{-3} . As demonstrated in Fig. 7(d), maintaining a thickness among 0.1 and 2.0 μm and keeping the N_t equal to 10^{12} cm^{-3} results in the optimal conversion efficiency, which exceeds 17.12%.

In contrast, the performance metrics of the Al/FTO/CdS/ Ba_3SbCl_3 /Au (device IV) structures degrade as the PCE drops from 17.45% to 2.55%, the FF from 76% to 52.4%, the J_{SC} from 47.2 to 28.45 mA cm^{-2} , and the V_{OC} from 0.49 to 0.17 V. Fig. 8(a) shows that the peak V_{OC} of 0.46 V is reached once the N_t is below 10^{12} cm^{-3} and the absorber layer thickness is below 1 μm . However, exceeding this N_t threshold significantly reduces the V_{OC} to 0.19 V. Fig. 8(b) and (c) suggest that to achieve the highest J_{SC} and FF values of 45.55 mA cm^{-2} and 74.49%, the thickness should exceed 1 μm and the N_t should remain under 10^{12} cm^{-3} . Fig. 8(d) indicates that maintaining a thickness ranging from 0.1 to 2.0 μm and keeping the N_t equal to 10^{12} cm^{-3} results in the optimal conversion efficiency, which exceeds 15.71%.

3.8. Impact of device thickness (I, II, III, and IV) and interface change in solar energy efficiency

Fig. 9 presents the influence of N_{int} on the outcome of photovoltaic cells, illustrating alterations in the N_{int} as well as the

thickness of the Ba_3NCl_3 absorber layer. These parameters range from 10^{10} to 10^{18} cm^{-3} for defect density and 0.1 to 2.0 μm for thickness. The metrics for solar cell performance reduces significantly if the N_{int} in the Ba_3NCl_3 interface exceeds 10^{12} cm^{-3} . The J_{SC} , V_{OC} , PCE, and FF of Al/FTO/CdS/ Ba_3NCl_3 /Au structures reduce from 64.5 to 42 mA cm^{-2} , 0.57 V to 0.15 V, 24.9% to 2.4%, and 77% to 37.8%, respectively.

Fig. 9(a) shows that the peak V_{OC} of 0.5 V is gained while the absorber layer is 1 μm thick and the N_{int} is below 10^{12} cm^{-3} . However, exceeding this threshold of the N_{int} significantly reduces the V_{OC} to 0.16 V. Fig. 9(b) and (c) indicate that to achieve the peak J_{SC} of 53.97 mA cm^{-2} and FF of 82.06%, the absorber thickness should be larger than 1 μm , and the N_{int} should remain below 10^{12} cm^{-3} . Fig. 9(d) depict that the highest conversion efficiency, surpassing 23.06%, occurs within a thickness ranging from 0.1 to 2.0 μm and when N_{int} is equal to 10^{12} cm^{-3} . The addition of high-defect states to the absorber layer boosts carrier recombination, causing a decline in total cell performance.^{77–79} The best conditions for attaining the peak PCE of 23.06% for device I were identified, which includes a constant Ba_3NCl_3 absorber thickness of 1.0 μm and an N_{int} of 10^{12} cm^{-3} . A V_{OC} of 0.5 V, a J_{SC} of 53.97 mA cm^{-2} ,

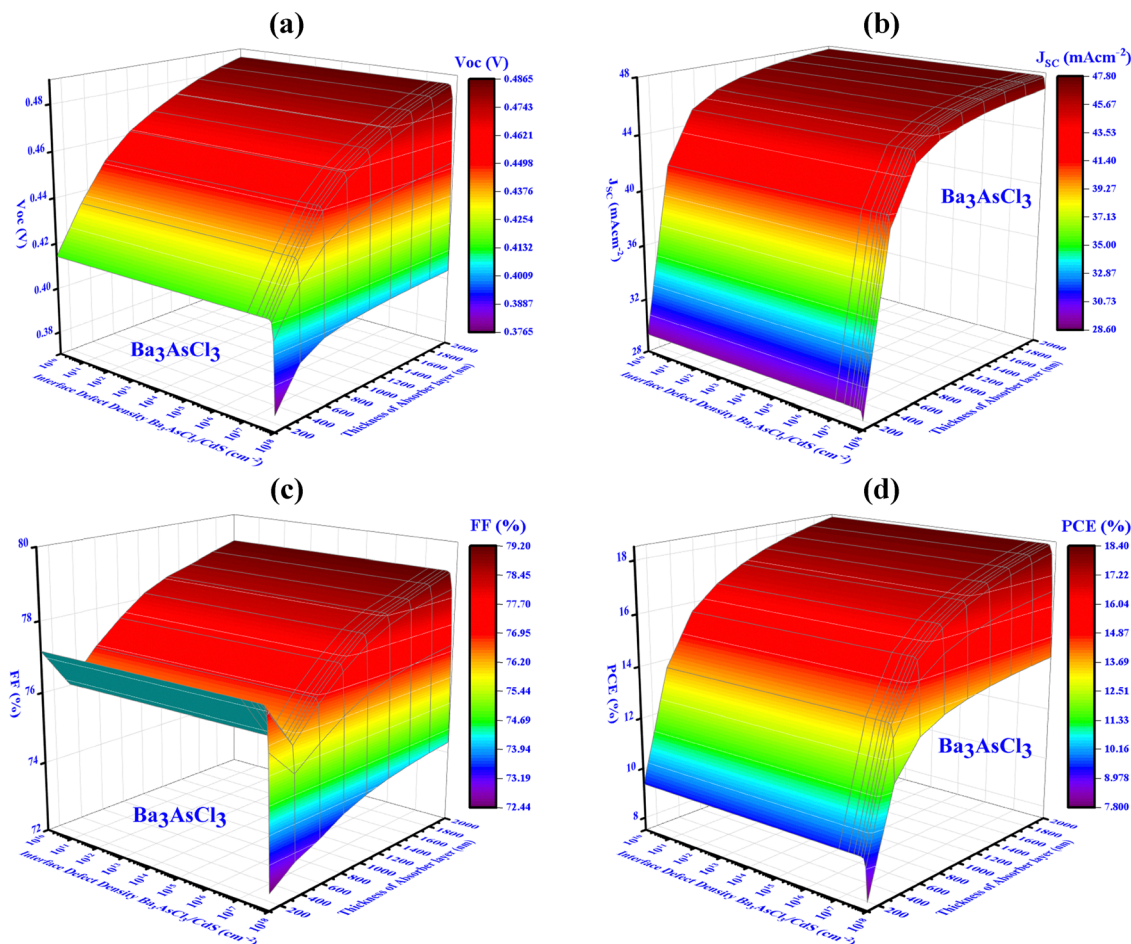


Fig. 11 Influence of variations in absorber thickness and defect interface density (device-III, Ba_3AsCl_3) on key PV performance factors: (a) V_{OC} , (b) J_{SC} , (c) FF, and (d) PCE.

and an FF of 82.06% were achieved by the solar cell in this case.

For Al/FTO/CdS/Ba₃PbCl₃/Au (device II) structures, performance factors such as J_{SC} , PCE, V_{OC} , and FF are negatively impacted by a rise in interface defect density, while an upsurge in the absorber layer's thickness generally improves these values. Up to a thickness of 1 μm , these parameters increase significantly. However, beyond 1 μm , the improvements are marginal. Similarly, these values decrease significantly as the N_{int} rises up to 10^{12} cm^{-3} , but the reduction is more gradual once the N_{int} surpasses 10^{12} cm^{-3} . Therefore, the optimal thickness is 1 μm , and the ideal N_{int} is 10^{12} cm^{-3} . Under these conditions, the PCE is 19.93%, the FF is 80.01%, the J_{SC} is 50.78 mA cm^{-2} , and the V_{OC} is 0.49 V. As illustrated in Fig. 10(a), the peak V_{OC} of 0.49 V is gained with a thickness below 1 μm and a N_{int} under 10^{12} cm^{-3} . However, exceeding this interface defect density threshold significantly reduces the V_{OC} to 0.32 V. Fig. 10(b) and (c) indicate that to reach the greatest values of J_{SC} (50.78 mA cm^{-2}) and FF (80.01%), the thickness should be superior to 1 μm and the N_{int} should not exceed 10^{12} cm^{-3} . According to Fig. 10(d), maintaining a thickness between 0.1 and 2.0 μm and an N_{int} equal to

10^{12} cm^{-3} results in the optimal conversion efficiency, which exceeds 19.93%.

The J_{SC} , V_{OC} , PCE, and FF of Al/FTO/CdS/Ba₃AsCl₃/Au (device-III) structures decrease from 47.8 to 28.6 mA cm^{-2} , 0.49 to 0.38 V, 18.4 to 7.8%, and 79.2 to 72.44%, respectively. Fig. 11(a) shows that the peak V_{OC} of 0.47 V is gained if the thickness is below 1 μm and the N_{int} is under 10^{12} cm^{-3} . However, exceeding this interface defect density threshold significantly reduces the V_{OC} to 0.39 V. Fig. 11(b) and (c) show that the thickness needs to exceed 1 μm and the N_{int} should not exceed 10^{12} cm^{-3} to attain the peak J_{SC} and FF values of 46.76 mA cm^{-2} and 78.15%, respectively. Fig. 11(d) shows that a thickness ranging from 0.1 to 2.0 μm and a N_{int} equal to 10^{12} cm^{-3} result in the maximum efficiency, exceeding 17.12%.

The FF, J_{SC} , PCE, and V_{OC} of the Al/FTO/CdS/Ba₃SbCl₃/Au (device IV) structures decrease from 76 to 55.8%, 47.2 to 28.15 mA cm^{-2} , 17.45 to 2.6%, and 0.49 to 0.17 V, respectively. Fig. 12(a) shows that the highest V_{OC} of 0.46 V is reached if the thickness is below 1 μm and N_{int} is under 10^{12} cm^{-3} . Besides, when the N_{int} exceeds 10^{12} cm^{-3} , the V_{OC} noticeably falls into 0.19 V. Fig. 12(b) and (c) indicate that the thickness needs to exceed 1 μm and the N_{int} should not exceed 10^{12} cm^{-3} to

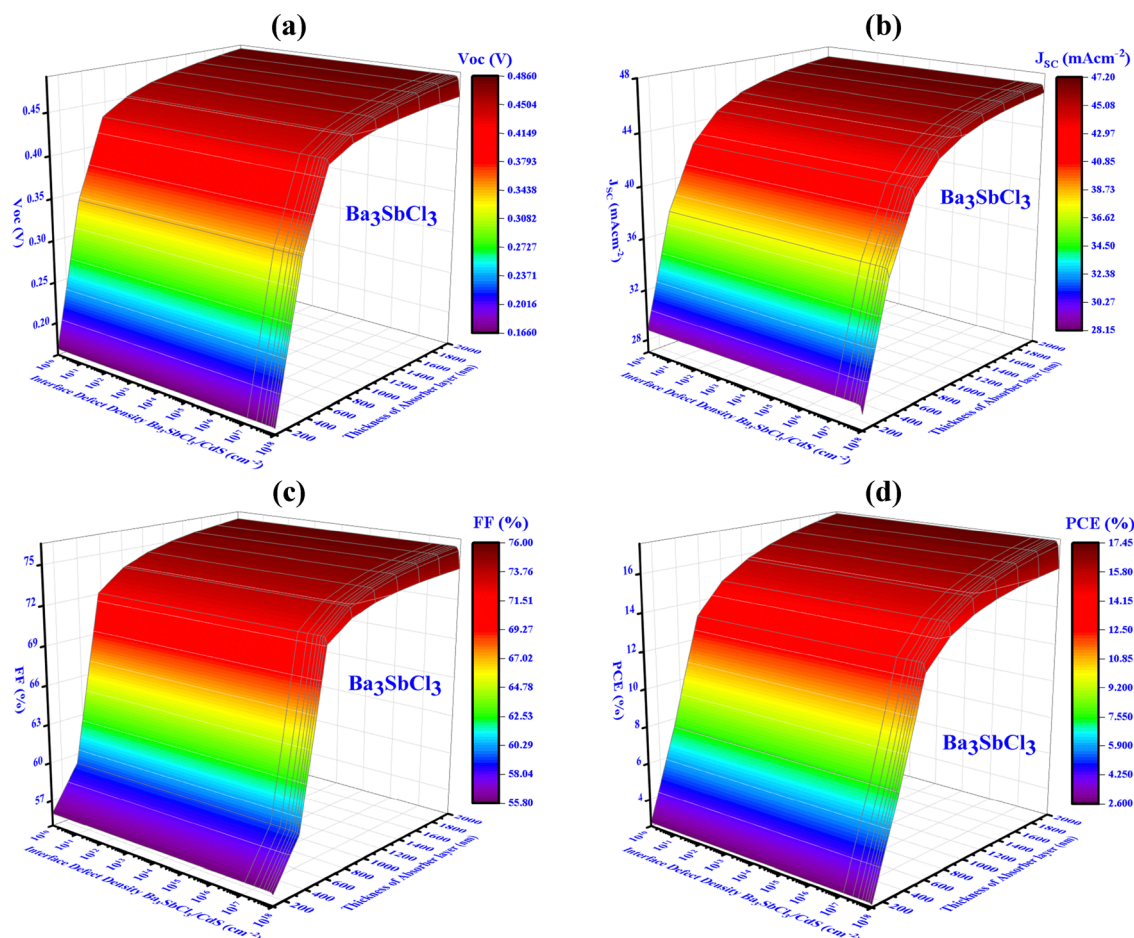


Fig. 12 Influence of variations in absorber thickness and defect interface density (device-IV, Ba₃SbCl₃) on key PV performance factors: (a) V_{OC} , (b) J_{SC} , (c) FF, and (d) PCE.

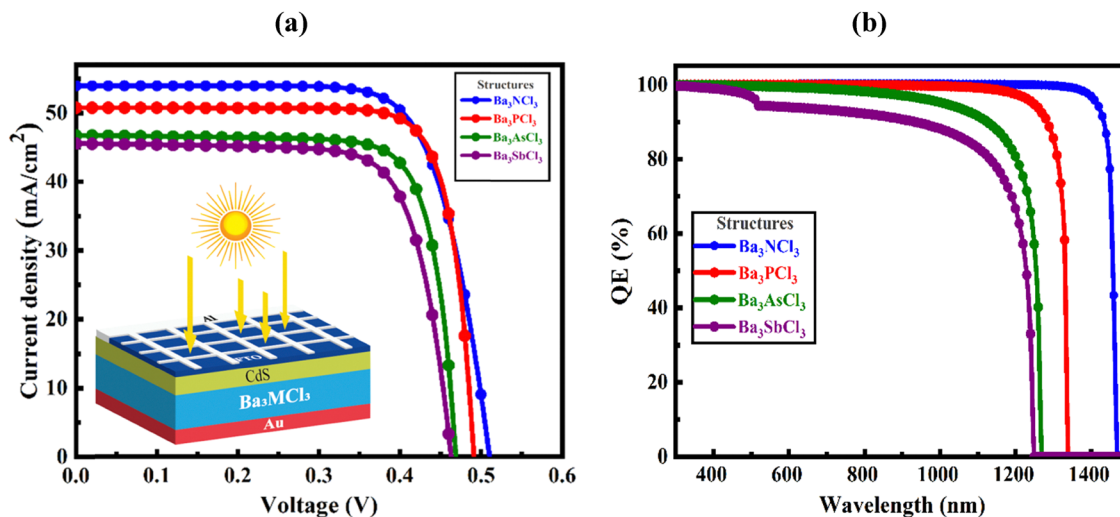


Fig. 13 (a) J - V and (b) PSC QE curves for devices I, II, III, and IV.

achieve the highest J_{SC} and FF values of 45.55 mA cm^{-2} and 74.49%, respectively. Fig. 12(d) demonstrates that a thickness spanning from 0.1 to $2.0 \mu\text{m}$ and an N_{int} equal to 10^{12} cm^{-3} result in the utmost efficiency, exceeding 15.71%.

As absorber thickness increases, more incident photons are absorbed due to the longer optical path, enhancing light absorption. However, beyond a certain point, further thickness results in only marginal gains, as absorption approaches saturation, consistent with the Beer-Lambert law.⁸⁰ While thicker layers generate more carriers, they also increase the transport distance, leading to higher recombination, particularly if the carrier diffusion length is shorter than the absorber thickness. This trade-off affects overall efficiency, where thinner layers underperform in photon absorption, and excessively thick layers suffer from recombination losses.⁸¹ The optimal thickness, around 1000 nm, strikes a balance between maximizing photon absorption and minimizing recombination. According to Shockley-Read-Hall recombination theory,⁸² this intermediate thickness offers the highest efficiency by reducing recombination losses while maintaining strong absorption.

3.9. Optimized J - V and QE characteristics

The J - V curves for the device, with optimal parameters (N_A of 10^{16} cm^{-3} , N_{int} of 10^{12} cm^{-2} , N_t of 10^{12} cm^{-2}) and absorber thicknesses between 100 and 2000 nm, are shown in Fig. 13(a). Analysis determined 1000 nm as the ideal absorber thickness, yielding values of (V_{OC} : 0.5 V, J_{SC} : 53.97 mA cm^{-2} , FF: 82.06%), (V_{OC} : 0.49 V, J_{SC} : 50.78 mA cm^{-2} , FF: 80.06%), (V_{OC} : 0.47 V, J_{SC} : 46.76 mA cm^{-2} , FF: 78.15%), and (V_{OC} : 0.46 V, J_{SC} : 45.55 mA cm^{-2} , FF: 74.49%) for devices I, II, III and IV, respectively, with CdS producing the highest PCE. Fig. 13(b) shows the QE curve for absorber thicknesses from 100 to 2000 nm, where QE, the fraction of photogenerated charge carriers per incident photon,^{83–85} nearly reached saturation at 1000 nm, then rapidly dropped to zero at cutoff wavelengths of 1460, 1330, 1260, and 1240 nm for devices I, II, III and IV, respectively. The 1000-nm

thickness was deemed ideal, as supported by the QE spectra and J - V characteristics.

4. Conclusions

This study examines the impact of M-anion modifications on lead-free halide inorganic compounds, specifically Ba_3MCl_3 ($M = \text{N, P, As, Sb}$), using DFT and SCAPS-1D software. The analysis begins with the use of GGA and PBE functional theory. Band structure and DOS analyses confirm the semiconductor properties of Ba_3MCl_3 compounds ($M = \text{N, P, As, Sb}$). Optical features such as absorption, dielectric function, electrical conductivity, loss function, reflectance, and refractive index, are explored. ECD mapping reveals the ionic bond nature of these compounds. For the perovskite solar cell, the SCAPS simulator was used to design the structure $\text{Al/FTO/CdS}/(\text{Ba}_3\text{NCl}_3/\text{Ba}_3\text{PbCl}_3/\text{Ba}_3\text{AsCl}_3/\text{Ba}_3\text{SbCl}_3)/\text{Au}$. The simulation results show that Ba_3NCl_3 delivers the highest J_{SC} , V_{OC} , PCE, and FF values, with 53.97 mA cm^{-2} , 0.5 V, 23.06%, and 82.06%, respectively, outperforming other compounds under similar conditions. In contrast, Ba_3SbCl_3 exhibits the lowest output values, with J_{SC} of 45.55 mA cm^{-2} , V_{OC} of 0.46 V, PCE of 15.71%, and FF of 74.49%. These results indicate that Ba_3MCl_3 ($M = \text{N, P, As, Sb}$) compounds have promise for further research in optoelectronic applications.

List of abbreviations

J - V	Current density-voltage
N_t	Defect density
PCE	Power conversion efficiency
ECD	Electron charge density
SCAPS	Solar cell capacitance simulator
J_{SC}	Short circuit current density
QE	Quantum efficiency
VB	Valence band

V_{OC}	Open circuit voltage
ETL	Electron transport layer
SCF	Self-consistent field
DFT	Density functional theory
N_{int}	Interface defect density
BZ	Brillouin zone
FTO	Fluorine-doped tin oxide
PSC	Perovskite solar cell
FF	Fill factor
CB	Conduction band
HTL	Hole transport layer
WF	Work function
PV	Photovoltaic

Data availability

Data are available from the corresponding author upon reasonable request.

Conflicts of interest

The authors have no conflicts of interest.

Acknowledgements

A. Irfan extends his appreciation to the Deanship of Research and Graduate Studies at King Khalid University for funding this work through the Large Research Project under grant number RGP2/172/45.

References

- 1 S. Marimuthu, S. Pandiaraj, M. Muthuramamoorthy, K. E. Alzahrani, A. N. Alodhayb, S. Pitchaimuthu and A. N. Grace, Experimental and computational DFT, drift-diffusion studies of cobalt-based hybrid perovskite crystals as absorbers in perovskite solar cells, *Phys. Chem. Chem. Phys.*, 2024, **26**, 4262–4277.
- 2 C. Xing, Y. Lei, M. Liu, S. Wu, W. He and Z. Zheng, Environment-friendly Cu-based thin film solar cells: materials, devices and charge carrier dynamics, *Phys. Chem. Chem. Phys.*, 2021, **23**, 16469–16487.
- 3 C. Paduani and A. M. Rappe, Tuning the gap of lead-based halide perovskites by introducing superalkali species at the cationic sites of ABX_3 -type structure, *Phys. Chem. Chem. Phys.*, 2017, **19**, 20619–20626.
- 4 D. Liu, H. Zeng, H. Peng and R. Sa, Computational study of the fundamental properties of Zr-based chalcogenide perovskites for optoelectronics, *Phys. Chem. Chem. Phys.*, 2023, **25**, 13755–13765.
- 5 Y.-C. Zhao, W.-K. Zhou, X. Zhou, K.-H. Liu, D.-P. Yu and Q. Zhao, Quantification of light-enhanced ionic transport in lead iodide perovskite thin films and its solar cell applications, *Light: Sci. Appl.*, 2017, **6**, e16243–e16243.
- 6 D. Luo, W. Yang, Z. Wang, A. Sadhanala, Q. Hu, R. Su, R. Shivanna, G. F. Trindade, J. F. Watts, Z. Xu, T. Liu, K. Chen, F. Ye, P. Wu, L. Zhao, J. Wu, Y. Tu, Y. Zhang, X. Yang, W. Zhang, R. H. Friend, Q. Gong, H. J. Snaith and R. Zhu, Enhanced photovoltage for inverted planar heterojunction perovskite solar cells, *Science*, 2018, **360**, 1442–1446.
- 7 H. Bencherif and M. Khalid Hossain, Design and numerical investigation of efficient $(FAPbI_3)_{1-x}(CsSnI_3)_x$ perovskite solar cell with optimized performances, *Sol. Energy*, 2022, **248**, 137–148.
- 8 D. Nadhiya, A. Kala, P. Sasikumar, M. K. A. Mohammed, P. Thirunavukkarasu, M. Prabhakaran, C. Karnan, S. Albukhaty, M. S. Jabir, A. Syed, A. M. Elgorban and N. S. S. Zaghloul, Influence of Cu^{2+} substitution on the structural, optical, magnetic, and antibacterial behaviour of zinc ferrite nanoparticles, *J. Saudi Chem. Soc.*, 2023, **27**, 101696.
- 9 M. Mohammed, A. K. Al-Mousoi, S. M. Majeed, S. Singh, A. Kumar, R. Pandey, J. Madan, D. Ahmed and D. Dastan, Stable Hole-Transporting Material-Free Perovskite Solar Cells with Efficiency Exceeding 14% via the Introduction of a Malonic Acid Additive for a Perovskite Precursor, *Energy Fuels*, 2022, **36**, 13187–13194.
- 10 J. Jiang, Z. Jin, J. Lei, Q. Wang, X. Zhang, J. Zhang, F. Gao and S. (Frank) Liu, ITIC surface modification to achieve synergistic electron transport layer enhancement for planar-type perovskite solar cells with efficiency exceeding 20%, *J. Mater. Chem. A*, 2017, **5**, 9514–9522.
- 11 F. Meinardi, Q. A. Akkerman, F. Bruni, S. Park, M. Mauri, Z. Dang, L. Manna and S. Brovelli, Doped Halide Perovskite Nanocrystals for Reabsorption-Free Luminescent Solar Concentrators, *ACS Energy Lett.*, 2017, **2**, 2368–2377.
- 12 M. K. A. Mohammed, S. Singh, A. K. Al-Mousoi, R. Pandey, J. Madan, D. Dastan and G. Ravi, Improving the potential of ethyl acetate green anti-solvent to fabricate efficient and stable perovskite solar cells, *RSC Adv.*, 2022, **12**, 32611–32618.
- 13 L. Huxin, X. Liu, X. Gong, R. Zhou, X. Peng, Y. Ouyang, J. Zhuang, H. Li and H. Wang, Multifunctional Additive of Potassium Cinnamate Improve Crystallization and Passivate Defect for Perovskite Solar Cell with Efficiency Exceeding 22%, *Energy Technol.*, 2022, **10**, 2200125.
- 14 M. K. Hossain, G. F. I. Toki, A. Kuddus, M. H. K. Rubel, M. M. Hossain, H. Bencherif, M. F. Rahman, M. R. Islam and M. Mushtaq, An extensive study on multiple ETL and HTL layers to design and simulation of high-performance lead-free $CsSnCl_3$ -based perovskite solar cells, *Sci. Rep.*, 2023, **13**, 1–24.
- 15 Z. Shi, J. Guo, Y. Chen, Q. Li, Y. Pan, H. Zhang, Y. Xia and W. Huang, Lead-Free Organic-Inorganic Hybrid Perovskites for Photovoltaic Applications: Recent Advances and Perspectives, *Adv. Mater.*, 2017, **29**, 1605005.
- 16 X. Meng, Y. Wang, J. Lin, X. Liu, X. He, J. Barbaud, T. Wu, T. Noda, X. Yang and L. Han, Surface-Controlled Oriented Growth of $FASnI_3$ Crystals for Efficient Lead-free Perovskite Solar Cells, *Joule*, 2020, **4**, 902–912.
- 17 G. Schileo and G. Grancini, Lead or no lead? Availability, toxicity, sustainability and environmental impact of lead-free perovskite solar cells, *J. Mater. Chem. C*, 2021, **9**, 67–76.

- 18 N. Pandit, R. Singh, T. K. Joshi, A. Shukla, P. K. Kamlesh, A. Dubey, T. Kumar, M. S. Chauhan and A. S. Verma, Investigation of a potential photovoltaic absorber based on first principles spectroscopic screening of chalcogenide perovskites: CaZrX_3 ($X = \text{S}, \text{Se}$), *J. Comput. Electron.*, 2024, **24**, 11.
- 19 N. Pandit, R. Singh, P. K. Kamlesh, N. Kumar, P. Sharma, S. Kumari, T. Kumar, S. Al-Qaisi and A. S. Verma, Study of chalcogenide-based metal perovskites BaZrX_3 ($X = \text{S}$ and Se): DFT insight into fundamental properties for sustainable energy generation using AMPs-1D, *J. Comput. Electron.*, 2024, **23**, 1014–1028.
- 20 N. Pandit, R. Singh, A. Kumar, T. K. Joshi, A. Shukla, U. Rani, P. K. Kamlesh, T. Kumar, Priyanka and A. S. Verma, Physical properties and power conversion efficiency of SrZrX_3 ($X = \text{S}$ and Se) chalcogenide perovskite solar cell, *Mod. Phys. Lett. B*, 2024, **38**, 2450345.
- 21 S. Kumari, U. Rani, M. Rani, R. Singh, P. K. Kamlesh, S. Kumari, T. Kumar and A. S. Verma, Computational investigation of the fundamental physical properties of lead-free halide double perovskite $\text{Rb}_2\text{NaCoX}_6$ ($X = \text{Cl}, \text{Br}$, and I) materials: potential prospects for sustainable energy, *Mod. Phys. Lett. B*, 2024, **38**, 2450323.
- 22 N. Pandit, A. Dubey, T. K. Joshi, A. Shukla, U. Rani, P. K. Kamlesh, R. Gupta, T. Kumar, K. Kaur and A. S. Verma, Effect of anion (S^{2-} & Se^{2-}) replacement on photovoltaic properties in transition metal (Ba-Barium) chalcogenide perovskites, *Int. J. Mod. Phys. B*, 2024, 2550059.
- 23 H. Park, R. Mall, F. H. Alharbi, S. Sanvito, N. Tabet, H. Bensmail and F. El-Mellouhi, Exploring new approaches towards the formability of mixed-ion perovskites by DFT and machine learning, *Phys. Chem. Chem. Phys.*, 2019, **21**, 1078–1088.
- 24 Y. Zhou and A. Gray-Weale, A numerical model for charge transport and energy conversion of perovskite solar cells, *Phys. Chem. Chem. Phys.*, 2016, **18**, 4476–4486.
- 25 Y.-Q. Zhao, Q.-R. Ma, B. Liu, Z.-L. Yu and M.-Q. Cai, Pressure-induced strong ferroelectric polarization in tetra-phase perovskite CsPbBr_3 , *Phys. Chem. Chem. Phys.*, 2018, **20**, 14718–14724.
- 26 M. F. Rahman, M. M. Islam, M. R. Islam, A. Ghosh, M. A. Rahman, M. H. Rahman, M. A. I. Islam, M. A. Islam, H. Albalawi and Q. Mahmood, An investigation on strain-incited electronic and optical properties of novel inorganic cubic material Sr_3AsCl_3 , *J. Solid State Chem.*, 2023, **328**, 124341.
- 27 M. F. Rahman, M. H. Rahman, M. R. Islam, M. K. Hossain, A. Ghosh, M. S. Islam, M. M. Islam, M. Harun-Or-Rashid, H. Albalawi and Q. Mahmood, The optical and electronic properties of inorganic halide perovskite Sr_3NCl_3 under applied biaxial strain, *J. Mater. Sci.*, 2023, **58**, 13100–13117.
- 28 M. F. Rahman, M. A. I. Islam, M. R. Islam, M. H. Ali, P. Barman, M. A. Rahman, M. Harun-Or-Rashid, M. Hasan and M. K. Hossain, Investigation of a novel inorganic cubic perovskite Ca_3PI_3 with unique strain-driven optical, electronic, and mechanical properties, *Nano Select*, 2023, **4**, 632–645.
- 29 M. F. Rahman, M. A. Rahman, M. R. Islam, A. Ghosh, M. A. Bashar Shanto, M. Chowdhury, M. Al Ijazul Islam, M. H. Rahman, M. K. Hossain and M. A. Islam, Unraveling the strain-induced and spin-orbit coupling effect of novel inorganic halide perovskites of Ca_3AsI_3 using DFT, *AIP Adv.*, 2023, **13**, 085329.
- 30 A. Ghosh, M. F. Rahman, M. R. Islam, M. S. Islam, M. Amami, M. K. Hossain and A. B. Md Ismail, Inorganic novel cubic halide perovskite Sr_3AsI_3 : strain-activated electronic and optical properties, *Heliyon*, 2023, **9**, e19271.
- 31 C. Hadenfeldt and H. O. Vollert, Darstellung, thermisches Verhalten und Kristallstruktur des Calciumarsenidchlorids Ca_3AsCl_3 , *J. Inorg. Gen. Chem.*, 1982, **491**, 113–118.
- 32 C. Hadenfeldt and H. Herdejürgen, Darstellung, kristallstruktur und thermisches verhalten der calciumphosphidchloride $\text{Ca}_{2-x}\text{P}_{1-x}\text{Cl}_{1+x}$ ($0 \leq x \leq 0.18$) und Ca_3PCl_3 , *J. Less-Common Met.*, 1986, **124**, 93–103.
- 33 V. C. Hadenfeldt and W. Fester, Reindarstellung und thermische Stabilität von Calcium-phosphid- und -arsenidiodiden: Ca , PI , Ca , AsI , Ca , PI und Ca , AsI , *Anorg. Chem.*, 1982, **30**, 25–30.
- 34 S. Andersson, Magnesium nitride fluorides, *J. Solid State Chem.*, 1970, **1**, 306–309.
- 35 C. Hadenfeldt and P. Schulz, Darstellung, Struktur und Temperaturabhängigkeit der Phasenbreite der Phase $\text{Ca}_{2-x}\text{As}_{1-x}\text{Br}_{1+x}$ und thermisches Verhalten der Verbindung Ca_3AsBr_3 , *J. Inorg. Gen. Chem.*, 1984, **518**, 77–86.
- 36 D. A. Dixon, in *Encyclopedia of Geochemistry*, ed. W. M. White, Springer International Publishing, Cham, 2016, pp. 1–7.
- 37 M. H. K. Rubel, M. A. Hossain, M. K. Hossain, K. M. Hossain, A. A. Khatun, M. M. Rahaman, M. Ferdous Rahman, M. M. Hossain and J. Hossain, First-principles calculations to investigate structural, elastic, electronic, thermodynamic, and thermoelectric properties of $\text{CaPd}_3\text{B}_4\text{O}_{12}$ ($\text{B} = \text{Ti}, \text{V}$) perovskites, *Results Phys.*, 2022, **42**, 105977.
- 38 M. F. Rahman, M. N. H. Toki, M. R. Islam, P. Barman, S. Chowdhury, M. Rasheduzzaman and M. Z. Hasan, A computational study of electronic, optical, and mechanical properties of novel Ba_3SbI_3 perovskite using DFT, *Opt. Quantum Electron.*, 2023, **56**, 206.
- 39 M. Ferdous Rahman, P. Barman, M. Azizur Rahman, M. Mushtaq, M. Rasidul Islam, M. Atikur Rahman, M. Z. Sultan, A. R. Chaudhry and A. Irfan, Electronic, optical, thermophysical, and mechanical properties of lead-free Ba_3SbBr_3 perovskite, *Polyhedron*, 2024, **254**, 116937.
- 40 Q. Wang, W. Yu, X. Fu, C. Qiao, C. Xia and Y. Jia, Electronic and magnetic properties of SnSe monolayers doped by Ga , In , As , and Sb : a first-principles study, *Phys. Chem. Chem. Phys.*, 2016, **18**, 8158–8164.
- 41 M. Faizan, J. Xie, G. Murtaza, C. Echeverría-Arrondo, T. Alshahrani, D. Bhamu, A. Laref, I. Seró and S. Khan, A first-principle study of the stability, electronic structure, and optical properties of halide double perovskite $\text{Rb}_2\text{Sn}_{1-x}\text{Te}_x\text{I}_6$ for solar cell applications, *Phys. Chem. Chem. Phys.*, 2023, **23**, 4646–4657.
- 42 M. D. Segall, P. J. D. Lindan, M. J. Probert, C. J. Pickard, P. J. Hasnip, S. J. Clark and M. C. Payne, First-principles

- simulation: ideas, illustrations and the CASTEP code, *J. Phys.: Condens. Matter*, 2002, **14**, 2717–2744.
- 43 W. Kohn and L. J. Sham, Self-Consistent Equations Including Exchange and Correlation Effects, *Phys. Rev. A: At., Mol., Opt. Phys.*, 1965, **140**, 1133.
 - 44 G. P. Francis and M. C. Payne, Finite basis set corrections to total energy pseudopotential calculations, *J. Phys.: Condens. Matter*, 1990, **2**, 4395–4404.
 - 45 T. H. Fischer and J. Almlöf, General methods for geometry and wave function optimization, *J. Phys. Chem.*, 1992, **96**, 9768–9774.
 - 46 J. P. Perdew, K. Burke and M. Ernzerhof, Generalized Gradient Approximation Made Simple, *Phys. Rev. Lett.*, 1996, **77**, 3865–3868.
 - 47 H. J. Monkhorst and J. D. Pack, Special points for Brillouin-zone integrations, *Phys. Rev. B: Condens. Matter Mater. Phys.*, 1976, **13**, 5188.
 - 48 M. H. Rahman, H. Full, M. A. Rahman, S. R. Al Ahmed, L. Ben Farhat, S. Ezzine and M. F. Rahman, ETL engineering in lead-free new Ca_3PBr_3 perovskite type structure of anti-perovskite derivative material for stable and effective photovoltaic solar cells, *New J. Chem.*, 2025, **49**, 3044–3066.
 - 49 S. Bhattacharyya and A. K. Singh, Semiconductor–metal transition in semiconducting bilayer sheets of transition-metal dichalcogenides, *Phys. Rev. B: Condens. Matter Mater. Phys.*, 2012, **86**, 1–7.
 - 50 W.-J. Yin, J.-H. Yang, J. Kang, Y. Yan and S.-H. Wei, Halide perovskite materials for solar cells: a theoretical review, *J. Mater. Chem. A*, 2015, **3**, 8926–8942.
 - 51 D.-Y. Chen, Y. Wu, L. Jin, Y. Li, X. Wang, J. Duan, J. Han, X. Li, Y.-Z. Long, X. Zhang, D. Chen and B. Teng, Superconducting properties in a candidate topological nodal line semimetal SnTaS_2 with a centrosymmetric crystal structure, *Phys. Rev. B*, 2019, **100**, 64516.
 - 52 M. Petrović, V. Chellappan and S. Ramakrishna, Perovskites: solar cells & engineering applications – materials and device developments, *Sol. Energy*, 2015, **122**, 678–699.
 - 53 M. A. Islam, M. Z. Rahaman and S. K. Sen, A comparative study of hydrostatic pressure treated environmentally friendly perovskites CsXBr_3 ($\text{X} = \text{Ge/Sn}$) for optoelectronic applications, *AIP Adv.*, 2021, **11**, 075109.
 - 54 M. A. Islam, J. Islam, M. N. Islam, S. K. Sen and A. K. M. A. Hossain, Enhanced ductility and optoelectronic properties of environment-friendly CsGeCl_3 under pressure, *AIP Adv.*, 2021, **11**, 45014.
 - 55 S. ur Rehman, F. K. Butt, Z. Tariq, F. Hayat, R. Gilani and F. Aleem, Pressure induced structural and optical properties of cubic phase SnSe : an investigation for the infrared/mid-infrared optoelectronic devices, *J. Alloys Compd.*, 2017, **695**, 194–201.
 - 56 F. Ahmad, A. Lakhtakia and P. B. Monk, Double-absorber thin-film solar cell with 34% efficiency, *Appl. Phys. Lett.*, 2020, **117**, 33901.
 - 57 D. Tsukahara, S. Yachi, H. Takeuchi, R. Takabe, W. Du, M. Baba, Y. Li, K. Toko, N. Usami and T. Suemasu, p-BaSi₂/n-Si heterojunction solar cells with conversion efficiency reaching 9.0%, *Appl. Phys. Lett.*, 2016, **108**, 152101.
 - 58 G. Yu, C. H. Lee, A. J. Heeger and S.-W. Cheong, Photoconductivity and optical conductivity in lightly doped $\text{Nd}_2\text{CuO}_{4-\delta}$, *Phys. C*, 1992, **203**, 419–425.
 - 59 M. A. Ali, N. Alam, S. Ali, S. A. Dar, A. Khan, G. Murtaza and A. Laref, A theoretical study of the structural, thermoelectric, and spin-orbit coupling influenced optoelectronic properties of CsTmCl_3 halide perovskite, *Int. J. Quantum Chem.*, 2020, **120**, 1–9.
 - 60 M. A. Ali, R. Ullah, S. Murad, S. A. Dar, A. Khan, G. Murtaza and A. Laref, Insight into pressure tunable structural, electronic and optical properties of via DFT calculations, *Eur. Phys. J. Plus*, 2020, **135**, 309.
 - 61 X. Liu, B. Xie, C. Duan, Z. Wang, B. Fan, K. Zhang, B. Lin, F. J. M. Colberts, W. Ma, R. A. J. Janssen, F. Huang and Y. Cao, A high dielectric constant non-fullerene acceptor for efficient bulk-heterojunction organic solar cells, *J. Mater. Chem. A*, 2018, **6**, 395–403.
 - 62 S. Saha, T. P. Sinha and A. Mookerjee, Electronic structure, chemical bonding, and optical properties of paraelectric BaTiO_3 , *Phys. Rev. B: Condens. Matter Mater. Phys.*, 2000, **62**, 8828–8834.
 - 63 M. M. Rahaman, M. H. K. Rubel, M. A. Rashid, M. A. Alam, K. M. Hossain, M. I. Hossain, A. A. Khatun, M. M. Hossain, A. K. M. A. Islam, S. Kojima and N. Kumada, Mechanical, electronic, optical, and thermodynamic properties of orthorhombic LiCuBiO_4 crystal: a first-principles study, *J. Mater. Res. Technol.*, 2019, **8**, 3783–3794, DOI: [10.1016/j.jmrt.2019.06.039](https://doi.org/10.1016/j.jmrt.2019.06.039).
 - 64 M. Roknuzzaman, K. (Ken) Ostrikov, K. Chandula Wasalathilake, C. Yan, H. Wang and T. Tesfamichael, Insight into lead-free organic-inorganic hybrid perovskites for photovoltaics and optoelectronics: a first-principles study, *Org. Electron.*, 2018, **59**, 99–106.
 - 65 M. Burgelman, P. Nollet and S. Degraeve, Modelling polycrystalline semiconductor solar cells, *Thin Solid Films*, 2000, **361–362**, 527–532.
 - 66 M. A. Ghebouli, B. Ghebouli, R. Larbi, T. Chihi and M. Fatmi, Effect of buffer nature, absorber layer thickness and temperature on the performance of CISSe based solar cells, using SCAPS-1D simulation program, *Optik*, 2021, **241**, 166203.
 - 67 A. Kuddus, M. F. Rahman, S. Ahmmed, J. Hossain and A. B. M. Ismail, Role of facile synthesized V_2O_5 as hole transport layer for CdS/CdTe heterojunction solar cell: validation of simulation using experimental data, *Superlattices Microstruct.*, 2019, **132**, 106168.
 - 68 U. Mandadapu, Simulation and Analysis of Lead based Perovskite Solar Cell using SCAPS-1D, *Indian J. Sci. Technol.*, 2017, **10**, 1–8.
 - 69 L. Lin, L. Jiang, P. Li, B. Fan and Y. Qiu, A modeled perovskite solar cell structure with a Cu_2O hole-transporting layer enabling over 20% efficiency by low-cost low-temperature processing, *J. Phys. Chem. Solids*, 2019, **124**, 205–211.
 - 70 I. Alam, R. Mollick and M. A. Ashraf, Numerical simulation of $\text{Cs}_2\text{AgBiBr}_6$ -based perovskite solar cell with ZnO nanorod

- and P3HT as the charge transport layers, *Phys. B*, 2021, **618**, 413187.
- 71 A. Bag, R. Radhakrishnan, R. Nekovei and R. Jeyakumar, Effect of absorber layer, hole transport layer thicknesses, and its doping density on the performance of perovskite solar cells by device simulation, *Sol. Energy*, 2020, **196**, 177–182.
 - 72 D. E. Tareq, S. M. AbdulMohsin and H. H. Waried, Efficiency of TiO_2 /Perovskites/ Cu_2O Solar Cells with Optimal Thickness at Varying of Environment Temperature, *IOP Conf. Ser.: Mater. Sci. Eng.*, 2020, **928**, 072044.
 - 73 D. Liu, M. K. Gangishetty and T. L. Kelly, Effect of $\text{CH}_3\text{NH}_3\text{PbI}_3$ thickness on device efficiency in planar heterojunction perovskite solar cells, *J. Mater. Chem. A*, 2014, **2**, 19873–19881.
 - 74 P. K. Patel, Device simulation of highly efficient eco-friendly $\text{CH}_3\text{NH}_3\text{SnI}_3$ perovskite solar cell, *Sci. Rep.*, 2021, **11**, 3082.
 - 75 A. Tara, V. Bharti, S. Sharma and R. Gupta, Device simulation of FASnI_3 based perovskite solar cell with $\text{Zn}(\text{O}_{0.3}, \text{S}_{0.7})$ as electron transport layer using SCAPS-1D, *Opt. Mater.*, 2021, **119**, 111362.
 - 76 K. D. Jayan and V. Sebastian, Comparative performance analysis of mixed halide perovskite solar cells with different transport layers and back metal contacts, *Semicond. Sci. Technol.*, 2021, **36**, 065010.
 - 77 M. Samiul Islam, K. Sobayel, A. Al-Kahtani, M. A. Islam, G. Muhammad, N. Amin, M. Shahiduzzaman and M. Akhtaruzzaman, Defect Study and Modelling of SnX_3 -Based Perovskite Solar Cells with SCAPS-1D, *Nanomaterials*, 2021, **11**, 1218.
 - 78 G. K. Gupta, A. Garg and A. Dixit, Electrical and impedance spectroscopy analysis of sol-gel derived spin coated $\text{Cu}_2\text{ZnSnS}_4$ solar cell, *J. Appl. Phys.*, 2018, **123**, 013101.
 - 79 F. Ferdiansjah and K. Tirtakusuma Mularso, Analysis of Back Surface Field (BSF) Performance in P-Type And N-Type Monocrystalline Silicon Wafer, *E3S Web Conf.*, 2018, **43**, 01006.
 - 80 M. A. Green, K. Emery, Y. Hishikawa, W. Warta and E. D. Dunlop, Solar cell efficiency tables (Version 45), *Prog. Photovoltaics Res. Appl.*, 2015, **23**, 1–9.
 - 81 S. Rühle, Tabulated values of the Shockley–Queisser limit for single junction solar cells, *Sol. Energy*, 2016, **130**, 139–147.
 - 82 W. Shockley and W. T. Read, Statistics of the Recombinations of Holes and Electrons, *Phys. Rev.*, 1952, **87**, 835–842.
 - 83 G. E. Eperon, G. M. Paternò, R. J. Sutton, A. Zampetti, A. A. Haghighirad, F. Cacialli and H. J. Snaith, Inorganic caesium lead iodide perovskite solar cells, *J. Mater. Chem. A*, 2015, **3**, 19688–19695.
 - 84 J. Hossain, M. M. A. Moon, B. K. Mondal and M. A. Halim, Design guidelines for a highly efficient high-purity germanium (HPGe)-based double-heterojunction solar cell, *Opt. Laser Technol.*, 2021, **143**, 107306.
 - 85 M. M. A. Moon, M. H. Ali, M. F. Rahman, A. Kuddus, J. Hossain and A. B. M. Ismail, Investigation of thin-film p-BaSi₂/n-CdS heterostructure towards semiconducting silicide based high efficiency solar cell, *Phys. Scr.*, 2020, **95**, 035506.